NOISE, HIGH-FREQUENCY

The high-frequency behavior of electronic devices is of major interest in the field of research and development. In addition to the typical RF device parameters, such as the cutoff frequency of the current gain, f_T, and the maximum frequency of oscillation, f_{max}, high-frequency noise behavior must be considered for circuit design, especially if noise has a significant influence on system performance, for example, the sensitivity of receivers. Thus there is a demand for simple, but exact RF noise models that have to consider the physically relevant noise phenomena making a significant contribution to the total noise behavior of the device.

After an introduction to various physical noise sources a standard description of noisy two-port circuits will be given. Next, a short presentation of a special setup for RF noise measurements in the range of 2 GHz to 18 GHz in relation to temperature (15 K to 400 K) is given. Radio-frequency noise phenomena in special devices are then examined, and high-frequency noise models for heterostructure field-effect transistors (HFETs) and heterojunction bipolar transistors (HBTs) based on the system material InP are presented. In the case of the HFET the capability of the model presented here will be proven with the help of a comparison between measured and modeled RF noise parameters. In the last section modifications of the noise model and applications of this RF noise model are presented.

NOISE THEORY

Physical Noise Sources

In this section only physical noise sources which are relevant for the high-frequency noise behavior of the devices will be described. Low-frequency noise phenomena, such as conductivity noise or $1/f$ noise, will not be considered.

Thermal Noise. The most important and well-known noise mechanism is thermal noise or *Johnson noise* (1,2). This process can be observed in all electrically conductive materials. Assuming a finite temperature T ($T > 0$ K), the free electrons randomly move in these materials forced by their thermal energy. Owing to scattering processes at lattice atoms, this movement leads to a statistical fluctuation of the voltage at the terminals of the conductor (e.g., a resistor R). The corresponding noise spectrum of the thermal noise is given as (1)

$$S_{\mathrm{th}}(f) = 4kTR \tag{1}$$

where k is Boltzmann's constant ($k = 1.38 \times 10^{-23}$ W·s/K). The measurable mean square values of the thermal noise current $\overline{i^2_{\mathrm{th}}(t)}$ and the thermal noise voltage $\overline{v^2_{\mathrm{th}}(t)}$ per unit bandwidth Δf are given as (3,4)

$$\overline{i^2_{\mathrm{th}}(t)} = 4kT\frac{\Delta f}{R} \tag{2}$$

and

$$\overline{v^2_{\mathrm{th}}(t)} = 4kTR\Delta f \tag{3}$$

respectively.

Shot Noise. The phenomenon of statistical current fluctuations is called *shot noise.* Because of the quantization of electron charge e, the electron flow, which corresponds to the number of electrons per unit time, is not continuous. Using these assumptions it is possible to divide a current $i(t)$ into a dc component I_0 and an ac component $i_{\mathrm{ac}}(t)$. Assuming Z is the average number of electrons per unit time, $i(t)$ can be written as

$$i(t) = I_0 + i_{\mathrm{ac}}(t), \qquad I_0 = Ze \tag{4}$$

The noise contribution caused by the ac current $i_{\mathrm{ac}}(t)$ is interpreted as an *ergodic* fluctuation phenomenon. A typical device dominated by shot noise is a vacuum diode with a pure metal cathode. However, the derived relations for this device can be applied to most semiconductor devices, too. For those frequencies, which are small compared with the reciprocal time period $1/\tau$ of the discrete current pulses, the single spectral contributions of each current pulse to the total noise spectrum can be neglected. In this case the so-called *Schottky relation* is valid for the spectrum of shot noise:

$$S_{\mathrm{S}}(f) = 2eI_0 \tag{5}$$

This spectrum is directly proportional to the mean dc current I_0 through the device. Generally, the *Schottky relation* is valid even for high-speed semiconductor devices and at very high frequencies. Equation (5) is also suitable to describe the related noise contribution due to gate-leakage current I_{leak} in the case of field-effect transistors if I_0 is replaced by I_{leak}.

Avalanche Noise. Charge-carrier multiplication in semiconductor devices can occur in regions of high electric field strengths. If the mean free path of carriers is long enough to

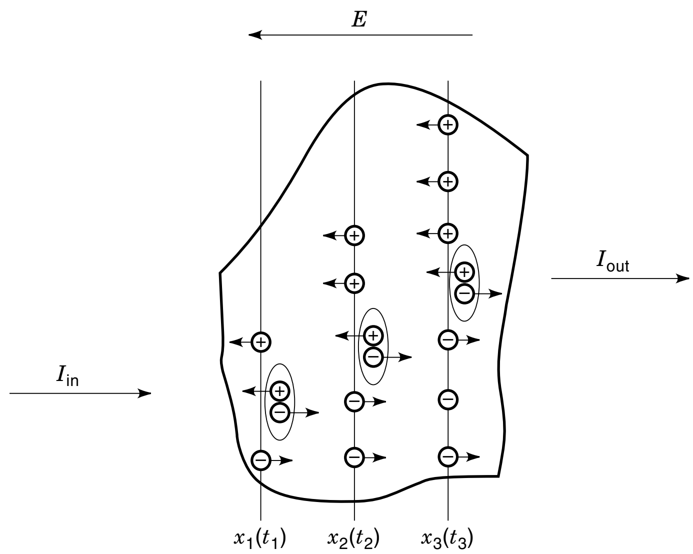

Figure 1. Model for the avalanche region at different locations and related time steps $x_i(t_i)$ with input current I_{in} and output current I_{out}.

achieve sufficient energy, additional electron–hole pairs are generated when colliding with lattice atoms (Fig. 1). This avalanche-like increase in the number of carriers often leads to a nonreversible degeneration of the device, known as *avalanche breakdown,* which is an electric breakdown mechanism. It is comparable to *thermal breakdown,* which is thermally activated carrier generation. Here, due to high electric field strengths only carrier generation is taken into account. If the increase in the number of carriers is limited, it becomes reversible and is often utilized to obtain special device performances as in *avalanche photodiodes* (APDs). In these devices the multiplication of optically generated electron–hole pairs enables a significant increase in optical responsivity, hence receiver sensitivity. The corresponding noise contribution is called *avalanche noise.* The avalanche noise is characterized by two ionization factors, for electrons α, and for holes β, which describe the number of carriers generated per unit length. They are dependent on the location and electric field strength, respectively. Assuming that the input current I_{in} shows shot noise and that the ionization coefficients for electrons and holes are equal ($\alpha = \beta$), the following expression for the noise spectrum of the output current I_{out} can be derived (5):

$$S_{I_{\mathrm{out}}} = 2eI_{\mathrm{in}}M^3 \tag{6}$$

where M is the avalanche multiplication factor.

If the ionization coefficients are different, but linearly dependent such as

$$\beta = c\alpha, \qquad c = \mathrm{const} \tag{7}$$

and the input current I_{in} is caused by electrons only, the spectrum of the output current is derived (6,7) as

$$S_{I_{\mathrm{out}}} = 2eI_{\mathrm{in}}M^3\left[1 - (1-c)\left(\frac{M-1}{M}\right)^2\right] \tag{8}$$

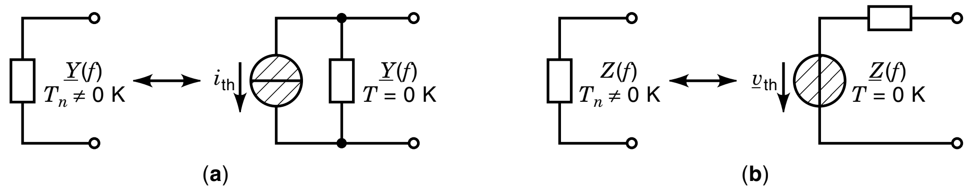

Figure 2. Equivalent circuits of noisy impedances or admittances: (a) noise current source and (b) noise voltage source.

In the case of a pure hole current, c has to be replaced by $1/c$ in Eq. (8). As partly mentioned before, two restrictions have to be considered for the validity of both relations:

1. The spectrum of the injected current I_{in} corresponds to that of shot noise only.
2. The length of the ionization region l_z is sufficient to achieve a high probability of collisions of the injected electrons with lattice atoms.

A modified relation is applicable to the phenomenon of impact ionization, which is of interest in conjunction with heterostructure FETs (see "Impact Ionization Noise in HFETs").

Noise in Linear Two-Port Circuits

Equivalent Circuits for Noisy Impedances and Admittances. For physically related noise modeling of devices a more generalized description of the single physical noise sources is necessary. The usual tool for noise calculations is the equivalent-circuit description, well known from RF modeling of devices. In the particular case of noise modeling all elements have to be treated as complex values.

Therefore only devices assimilating real power are able to emit thermal noise power (8). Replacing the real value R by the complex impedance $\underline{Z} = R + jX$ leads to the following equations for the measurable frequency-dependent mean square values of the thermal noise currents $\overline{i_{th}^2(t)}$ and noise voltages $\overline{v_{th}^2(t)}$ per unit bandwidth Δf. (Note that throughout this article complex numbers are underlined.)

$$\overline{i_{\text{th}}^2(t)} = 4kT\frac{\Delta f}{\text{Re}\{\underline{Z}\}} \tag{9}$$

and

$$\overline{v_{\text{th}}^2(t)} = 4kT\Delta f\,\text{Re}\{\underline{Z}\} \tag{10}$$

respectively, where the operator Re{ } accesses the real part of the particular value.

In a similar way, more generalized relations for the thermal spectral noise densities can be derived using Eqs. (9) and (10) as

$$S_{\text{th},i} = \overline{i_{\text{th}}^2(t)}\frac{1}{\Delta f} = 4kT\frac{1}{\text{Re}\{\underline{Z}\}} = 4kT\,\text{Re}\{\underline{Y}\} \tag{11}$$

and

$$S_{\text{th},v} = \overline{v_{\text{th}}^2(t)}\frac{1}{\Delta f} = 4kT\frac{1}{\text{Re}\{\underline{Y}\}} = 4kT\,\text{Re}\{\underline{Z}\} \tag{12}$$

Finally, this leads to a description of physical noise processes based on a small-signal equivalent circuit. The individual noisy impedances or admittances can be described by two compatible equivalent circuits (Fig. 2):

1. A noise current source $i_{th}(f)$ and a noise-free ($T = 0$ K) admittance in parallel
2. A noise voltage source $v_{th}(f)$ and a noise-free ($T = 0$ K) impedance in series

If the derived temperature of the impedance or admittance is different from the ambient temperature of the device it is called the equivalent noise temperature T_n.

Using this definition of the equivalent noise temperature, which is in the first instance valid for one-port circuits together with the derived equivalent RF circuits, enables one to calculate the noise behavior of complex circuits and systems. Typically, however, possible correlations among the individual noise sources of the total system have to be considered additionally.

The Noise Figure *F*. Unfortunately, the expression *noise figure,* which was originally defined for the description of noisy networks (9) and which is valid under certain assumptions only (cf. Ref. 10), sometimes leads to an overestimation of its real significance, especially in the case of discrete devices. Nevertheless, for systems the noise figure F is a more suitable parameter for noise characterization. If we speak about noise figure the formally defined *standard noise figure* F is implied, which assumes an input noise signal that is not arbitrarily given but related to the reference noise temperature of $T_0 = 290$ K, hence an absolute value (11).

By this means, the noise figure is a characteristic for the noise inherent in a two-port circuit, thus independent of external conditions or terminations of the ports. A noise-free two-port circuit is characterized by a noise figure of $F = 1$ or $F' = 0$ dB. Figure 3 shows the principal circuit description for the definition of the noise figure. It consists of a noisy two-port circuit connected to a load impedance $\underline{Z}_L$, assumed to be noise-free ($T = 0$ K). The input is connected to a noisy source impedance $\underline{Z}_S$ ($T > 0$ K). Again, this impedance is represented by a voltage noise source and a noise-free impedance $\underline{Z}_S$ ($T = 0$ K).

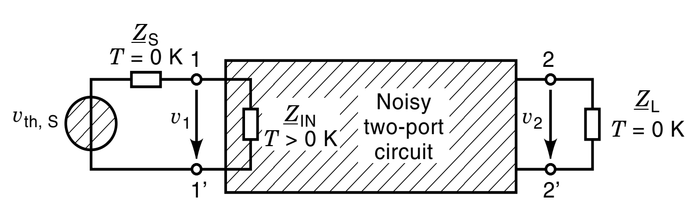

Figure 3. Equivalent circuit for the definition of the (standard) noise figure F.

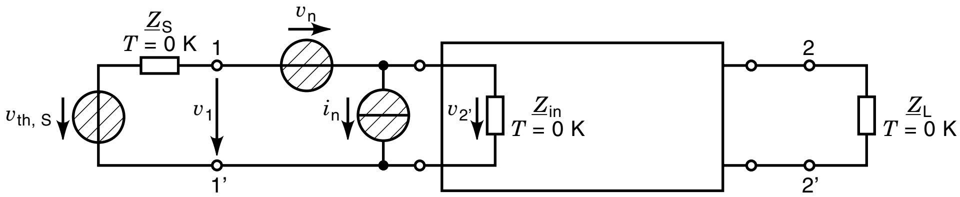

Figure 4. Noise equivalent circuit with noise current and noise voltage source "chained" at the input of the noise-free two-port circuit.

With S_{n2v} as the noise spectrum at the output of the noisy two-port circuit and S_{n20v} as the spectrum of the noise-free two-port circuit, F is defined by (8)

$$F = \frac{S_{n2v}}{S_{n20v}}; \quad F' = \log_{10}\frac{S_{n2v}}{S_{n20v}}\ \mathrm{dB} \tag{13}$$

An equivalent equation can be derived using the noise current spectra instead.

Calculation of the Noise Figure *F* Using Noise Equivalent Circuits. The noise figure F of noisy linear two-port circuits can be calculated using equivalent circuits (12,13). A very simple and suitable description for a noisy two-port circuit is the chain matrix or *ABCD*-parameter description, respectively, with one current noise source or one voltage noise source at the input terminal (Fig. 4). By this means, the noise behavior of the total two-port circuit can be modeled by two noise sources only, which are chained to the input.

Using this equivalent circuit for the noisy two-port circuit, the noise figure is given as

$$F = 1 + \frac{S_{nv} + |\underline{Z}_S|^2 S_{ni} + 2\,\mathrm{Re}\{\underline{Z}_S \underline{S}_{vi}\}}{4kT_0R_S} \tag{14}$$

where S_{nv} is the voltage noise spectrum, S_{ni} the current noise spectrum, and $\underline{S}_{vi}$ the cross-correlation spectrum between v_n and i_n.

The noise figure is independent of the input impedance of the two-port circuit $\underline{Z}_{in}$ and the load impedance $\underline{Z}_L$. However, the values of the spectra of the equivalent-noise-circuit sources of the two-port circuit as well as the cross-correlation spectrum, which describes the correlation between both noise sources, are required. Additionally, the noise figure depends on the source impedance $\underline{Z}_S$. The value of the noise figure reaches a minimum at $F = F_{min}$ for an optimal source impedance of $\underline{Z}_S = \underline{Z}_{S,opt}$. This is called *noise matching.* Unfortunately, the necessary impedances for noise matching differ from those for power matching. By this means, maximum available gain G_a of the two-port circuit is actually not available, and a reduced power gain, the so-called *associated gain* G_{assoc}, characterizes the two-port circuit. In designing electronic circuits, a compromise must always be made between noise and power matching.

Discussion of Noise Matching. As mentioned previously, the noise figure is a function of the source impedance $\underline{Z}_S$. Common measurement techniques for the determination of noise parameters are based on the relation given in Eq. (14). The dependence of F on deviations from the ideal matching condition can be described as in Ref. 10 by

$$F = F_{min} + \frac{R_n}{G_S}|\underline{Y}_S - \underline{Y}_{S,opt}|^2, \qquad \underline{Y}_S = G_S + jB_S \tag{15a}$$

or

$$F = F_{min} + \frac{g_n}{R_S}|\underline{Z}_S - \underline{Z}_{S,opt}|^2, \qquad \underline{Z}_S = \frac{1}{\underline{Y}_S} = R_S + jX_S \tag{15b}$$

using the equivalent noise conductance g_n with

$$g_n = R_n|\underline{Y}_{S,opt}|^2 \tag{16}$$

Obviously, just four parameters—the minimum noise figure F_{min}, the equivalent noise resistance R_n, and the real part $G_{S,opt}$ and the imaginary part $B_{S,opt}$ of the optimal generator (source) impedance—are necessary to describe the noise behavior of a linear two-port circuit completely.

R_n is a measure of the sensitivity of the noise figure to deviations from the optimum source admittance $\underline{Y}_{S,opt}$ or im-

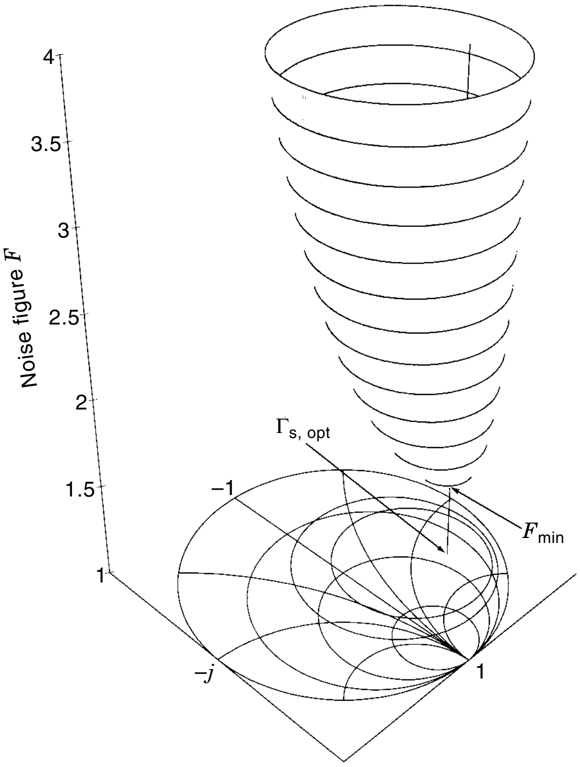

Figure 5. Noise figure F dependent on the generator reflection coefficient (here $F_{min} = 1.5$, $R_n = 50\ \Omega$, $|\underline{\Gamma}_{S,opt}| = \frac{2}{3}$, $\mathrm{Arg}\{\underline{\Gamma}_{S,opt}\} = 60°$).

pedance $\underline{Z}_{S,opt}$. By this means, R_n is a figure of merit for the noise behavior of the two-port circuit. The equivalent noise resistance should be as small as possible to avoid a significant increase in noise if, depending on the actual application, the optimum noise matching ($\underline{Y}_S = \underline{Y}_{S,opt}$) has to be sacrificed for a possibly more important power matching at the input.

Usually, the admittance or impedance is normalized and related to the characteristic impedance of the measurement setup $\underline{Z}_0$ ($\underline{Z}_0 = 50\ \Omega$, typically), which results in the following equation after transformation to the Smith-chart plane:

$$F = F_{\min} + 4r_n \frac{|\underline{\Gamma}_S - \underline{\Gamma}_{S,opt}|^2}{(1 - |\underline{\Gamma}_S|^2)|1 + \underline{\Gamma}_{S,opt}|^2} \tag{17}$$

where r_n is the normalized equivalent noise resistance ($r_n = R_n/\underline{Z}_0$), $\underline{\Gamma}_S$ the generator reflection coefficient, and $\underline{\Gamma}_{S,opt}$ the optimum generator reflection coefficient for noise matching.

Figure 5 shows a graphical interpretation of this equation, which characterizes a paraboloidal surface, in the Smith-chart plane. The minimum of the paraboloid represents the minimum noise figure $F_{\min}$ at the optimum generator reflection coefficient $\underline{\Gamma}_{S,opt}$. The latter can be derived by a perpendicular projection of the corresponding point onto the Smith-chart plane. If $\underline{\Gamma}_S$ differs from $\underline{\Gamma}_{S,opt}$ the noise figure F increases. As already discussed, this increase is directly proportional to the value of the equivalent noise resistance R_n, which corresponds to the slope of the paraboloid at a specific point. In practice, this circumstance could imply an even higher priority to achieve a low R_n than an absolutely low $F_{\min}$, depending on several boundary conditions to be still considered.

RF-NOISE MEASUREMENTS

Figure 6 shows a typical measurement setup, which allows temperature-dependent noise figure measurements of two-port circuits in the temperature range of 15 K to 400 K and frequency range of 2 GHz to 18 GHz (14,15). It comprises the noise figure meter (Hewlett-Packard Model No. HP8970B) as the central unit and the calibrated noise source (Model No. HP346A) (16). The noise figure test set (Model No. HP8971) and the synthesizer (Model No. HP8672A) are necessary to

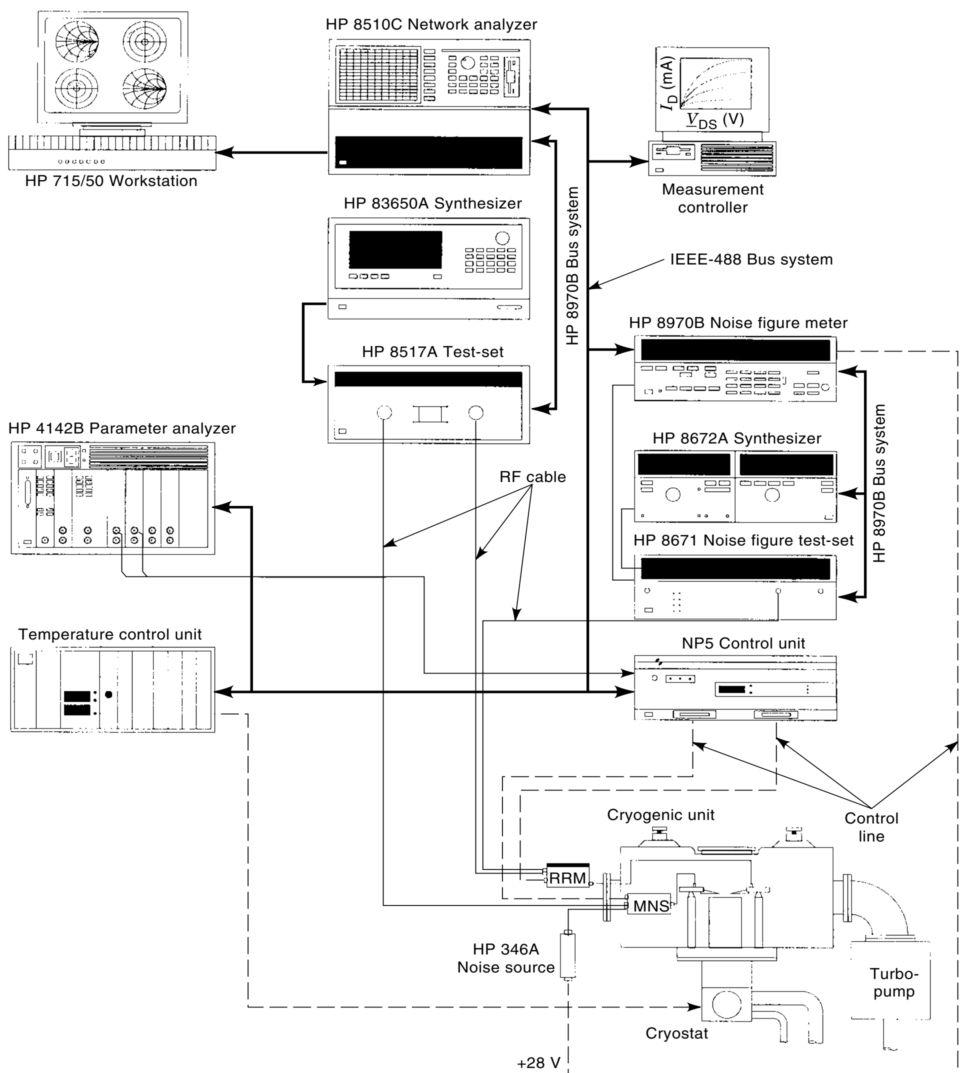

Figure 6. Measurement setup for RF-noise parameters in the range 2 GHz to 18 GHz dependent on temperature (15 K to 400 K). (Note: RRM = remote receiver module; MNS = mismatch noise source.)

down-convert the measurement frequency to a frequency range of 10 MHz to 1600 MHz, which the noise figure meter is able to process directly. To determine the four interesting noise parameters (F_{min}, R_n, $G_{S,opt}$, and $B_{S,opt}$) of a linear two-port circuit the noise figures at various generator reflection coefficients $\underline{\Gamma}_{S_i}$ have to be measured (17,18).

These particular reflection coefficients can be achieved using a commercial electronic tuner system (cf. Fig. 6). The tuner subsystem consists of the control unit (ATN Microwave Inc. Model No. NP5), the mismatch noise source (MNS), including the actual tuner, and the remote receiver module (RRM) with an integrated low noise preamplifier. Additionally, both elements (MNS and RRM) contain RF switches that are necessary for system calibration. Furthermore, these switches enable the simultaneous measurement of the noise and the corresponding scattering parameters. The complete system is controlled by a computer system that allows the evaluation of the data and the extraction of the specific noise parameters from the measured noise figures (16,19–22).

RF NOISE IN ELECTRONIC DEVICES

Noise in Heterostructure Field-Effect Transistors

Thermal Noise in HFET. The channel of a field-effect transistor (FET) can be interpreted as a controllable resistance. The thermal noise generated in this channel is the dominating noise contribution.

In case of an n-doped semiconductor, the well-known equation of the thermal noise current for a resistance R [cf. Eq. (2)] can be transformed into (23)

$$\overline{i_{\mathrm{th}}^2(t)} = 4kT_{\mathrm{eff}}\frac{1}{R_{\mathrm{ch}}}\,\Delta f \tag{18}$$

where T_{eff} is the effective temperature in the semiconductor channel and R_{ch} the resistance of the channel.

Considering geometrical aspects, the channel resistance can be expressed as

$$R_{\mathrm{ch}} = \frac{1}{\kappa}\frac{l}{A} \Rightarrow \frac{1}{R_{\mathrm{ch}}} = \kappa\frac{A}{\ell} \tag{19}$$

where A is the cross-sectional area of the channel and l the length of the current path through the semiconductor. The conductivity κ can be calculated for purely n-type (p-type) conductivity as

$$\kappa = en_0\mu_0 \tag{20}$$

where n_0 is the electron (hole) concentration and μ_0 the low-field mobility of electrons (holes). Moreover, the diffusion coefficient D_0 can be derived from Einstein's relation as

$$D_0 = \frac{kT\mu_0}{e} \tag{21}$$

Finally, this leads to a description of the thermal noise in the channel:

$$\overline{i_{\mathrm{th}}^2(t)} = 4e^2\,\frac{A}{l}\,n_0D_0\Delta f \tag{22}$$

In the case of high electric fields, as they occur in the region between the gate and drain, the conventional Einstein relation [Eq. (21)] is no longer valid. The diffusion coefficient and the low-field mobility as well as the effective noise temperature $T_{n,eff}$ of the channel become dependent on the electrical field strength E and the frequency f (24,25), leading to

$$\frac{kT_{\mathrm{n,eff}}(E,f)}{e} = \frac{D_0(E,f)}{\mathrm{Re}\{\underline{\mu}(E,f)\}} \tag{23}$$

Because of the relation between the thermal noise attributed to a resistor and the equivalent description for a semiconductor channel, it is often called *diffusion noise.*

Shot Noise in HFET. In principle, the shot noise of the drain current can be described using Eq. (5) (26,27). However, especially in heterostructure field-effect transistors, the recombination of carriers underneath the space-charge region leads to a significantly reduced shot noise (28,29).

Without further proof it can be assumed that the channel shot-noise contribution is negligible. Nevertheless, shot noise again becomes of major interest if the device suffers from gate leakage, which generates an additional noise contribution to the channel noise (see the section entitled "Shot Noise").

Impact Ionization Noise in HFET. The assumptions for avalanche noise as presented earlier are not valid in case of the HFET. Nevertheless, in the gate–drain region a type of avalanche noise occurs caused by impact ionization processes due to high electric field strengths. Especially in HFETs based on layers with an advanced carrier mobility (e.g., InGaAs), this additional noise contribution can be observed due to the low band gap of these channel materials. Typically, the area between gate and drain, where impact ionization can occur, is extremely small ($l \leq 100$ nm). Therefore, impact ionization leads to a moderate increase of the drain current I_D at high bias voltages V_{DS} only. The corresponding noise is called the impact ionization noise and differs from the basic avalanche noise because of the significantly smaller multiplication factor M [cf. Eq. (6)].

Using the same assumptions as in the case of the avalanche noise, but considering the special geometrical design of the HFET, the spectral density of the impact ionization noise $S_{I_{ii}}$ can be derived from (30,31):

$$S_{I_{\mathrm{ii}}} = M^2S_{I_{\mathrm{in}}} + 2eI_{\mathrm{in}}\sigma^2 \tag{24}$$

with $S_{I_{in}}$ being the density of the induced current I_{in} and σ^2 the variance of the noise process.

RF-Noise Model of InAlAs/InGaAs/InP HFET

Figure 7 shows a typical equivalent RF-noise model for InAlAs/InGaAs/InP HFET (32). It is based on an extended temperature noise model (TNM) (33), which takes into account the influence of gate-leakage current on both the RF and noise performance. Gate leakage is modeled by the additionally included resistances R_{PGD} and R_{PGS} in parallel to the intrinsic gate–drain elements and the intrinsic gate–source elements of the transistor, respectively. Moreover, this model considers the effects due to impact ionization (34,35). This is made possible by an additional voltage-controlled current

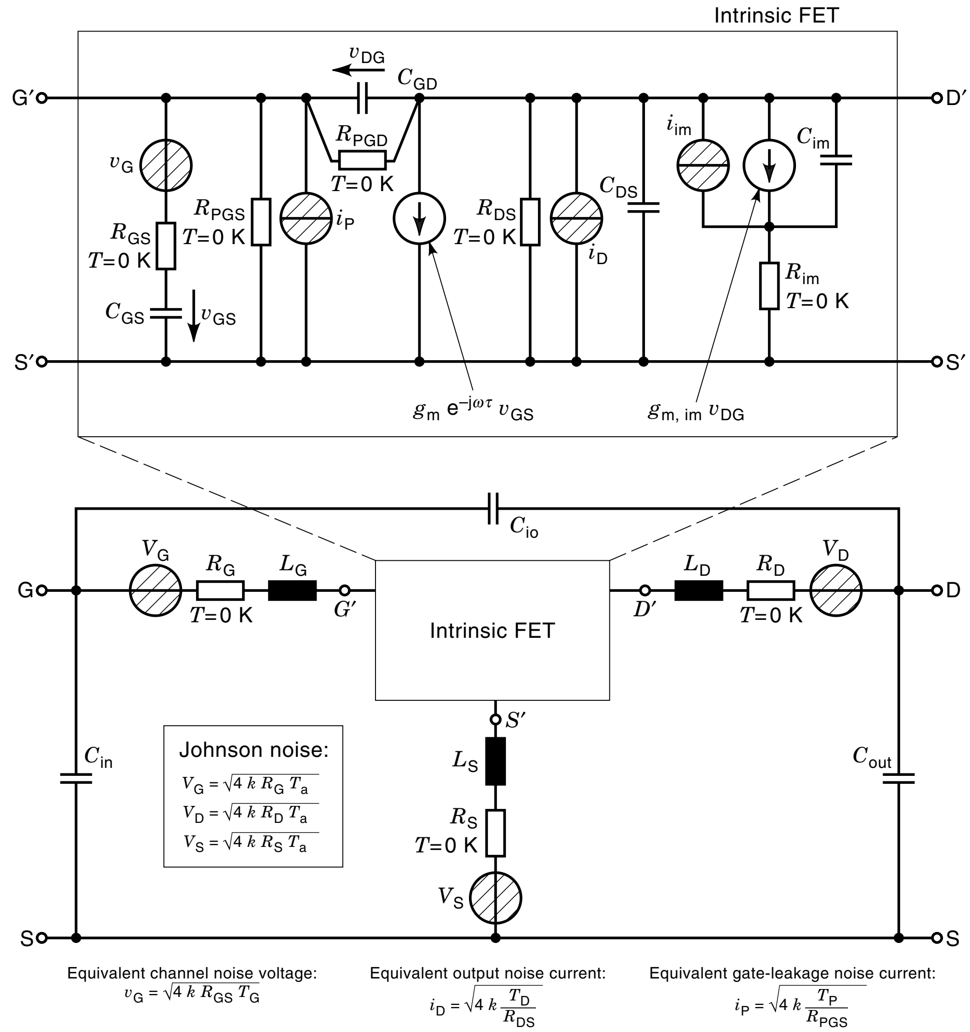

Figure 7. Intrinsic and extrinsic small-signal and noise equivalent circuit of HFET including modeling of the gate-leakage current and impact ionization on RF and noise behavior.

source $g_{m,im} \cdot v_{DG}$ and an RC combination in parallel with the output resistance. The current source is controlled by the voltage drop across the high-field region at the drain end of the gate, which is equal to the drain–gate voltage v_{DG}. The distinctive frequency dependence of the impact ionization effects on RF and noise behavior, respectively, are described by the combination of R_{im} and C_{im}. For noise modeling purposes an additional white noise source i_{im} is included parallel with the current source $g_{m,im} \cdot v_{DG}$. This arrangement of the noise source and RC combination characterizes the frequency dependence of the externally available noise current $i_{im,ext}$. This impact ionization source can be described by

$$\sqrt{\overline{i^2_{im,ext}}} = \sqrt{\overline{i^2_{im}}}\frac{1}{\sqrt{1 + (\omega/\omega_0)^2}}, \qquad \omega_0 = \frac{1}{R_{im}C_{im}} \tag{25}$$

The formula describes the Lorentzian shape of the external noise current which, typically, is attributed to carrier-generation processes, thus sustaining the previously noted interpretation of the occurrence of impact ionization (preceding section).

Thermally activated carrier-generation, especially from deep levels, also shows a Lorentzian-type spectrum, but usually at much lower frequencies, which makes it negligible in case of high-frequency noise.

The above described model is specific for InP HFET because both phenomena, gate-leakage current and impact ionization, occur in this device for special bias conditions. Other devices such as GaAs-HFET, MESFET, or MOSFET that do not show these phenomena can also be described with this model. In this particular case the equivalent elements that describe gate-leakage current and impact ionization have to be removed.

Noise in Heterojunction Bipolar Transistors

For the modeling of the high-frequency noise behavior of both bipolar junction transistors (BJTs) and heterojunction bipolar transistors (HBTs) the physical noise sources have to be defined in more detail. The most important noise phenomenon in all bipolar transistors is shot noise. In addition to this dominating effect, thermal noise due to the parasitic resistances has to be considered too.

Basically, a bipolar transistor consists of two combined p–n junctions. Figure 8 schematically shows the various current paths and components within an n–p–n bipolar transistor at active bias conditions. By this means, the base–emitter junction is biased forward, the base–collector junction reversely. The electron current from the emitter towards the collector [Fig. 8(a)] is the dominating current component.

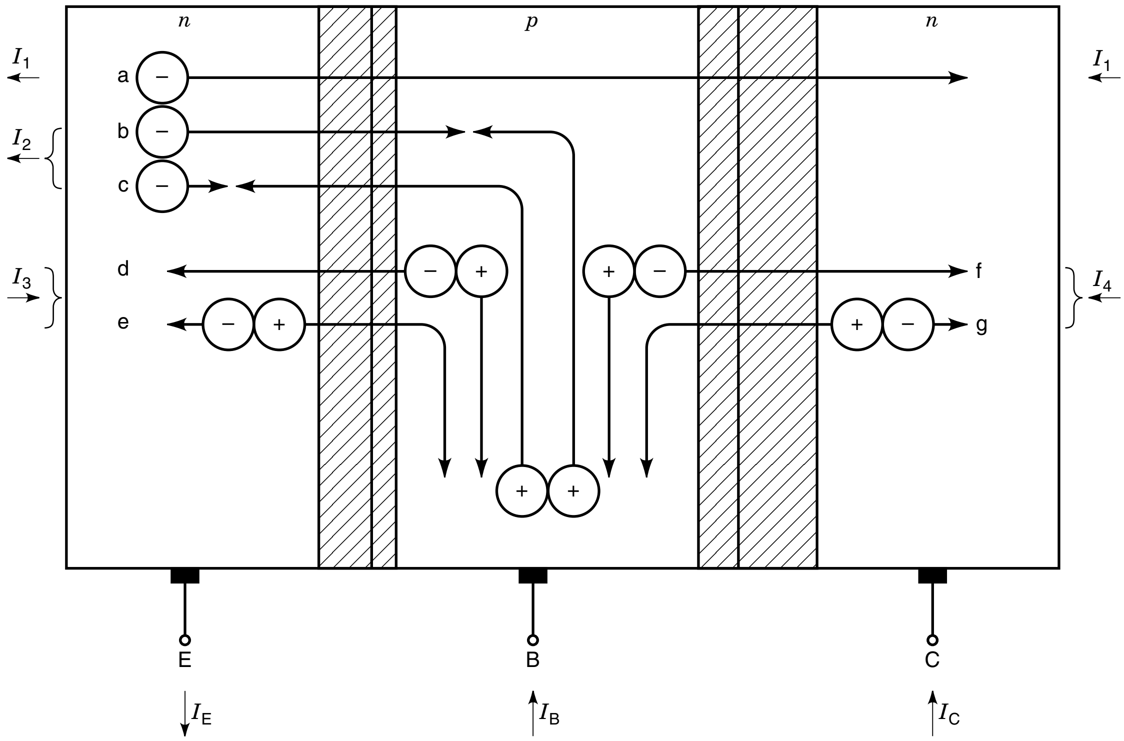

Figure 8. Current components and current flow in an n–p–n bipolar junction transistor.

Electrons induced from the emitter may recombine in the base, as described in Fig. 8(b). Holes are injected from the base into the emitter [Fig. 8(c)]. Electrons are thermally generated in the base and holes within the emitter, [Figs. 8(d) and 8(e), respectively].

In the case of the reverse-biased base–collector diode, only the current components due to the thermal generation of electron–hole pairs have to be taken into account [Figs. 8(f) and 8(g)]. All these current components can be combined, corresponding to Fig. 8, leading to four independent currents I_1, I_2,, I_3, and I_4.. The connection to the measureable currents at the terminals are then given as

$$I_E = I_1 + I_2 - I_3 \tag{26a}$$

$$I_C = I_1 + I_4 \tag{26b}$$

$$I_B = I_2 - I_3 - I_4 \tag{26c}$$

for the emitter, collector, and base, respectively.

With respect to noise modeling, the four current components can be represented by uncorrelated shot-noise sources leading to the simplified small-signal equivalent circuit (Fig. 9) (4). The shot noise corresponding to the dominating current I_1 is represented by two correlated shot-noise sources i_1' and i_1'' in the base–collector and the base–emitter regions, respectively. Both are related by the phase shift, which is given by α/α_0. α is the frequency-dependent current gain and α_0 the dc current gain for $f \to 0$ Hz.

$$i_1' = \sqrt{2eI_1\Delta f}\exp[j(\omega t + \varphi_1)] \tag{27a}$$

$$i_1'' = \frac{\alpha}{\alpha_0}\sqrt{2eI_1\Delta f}\exp[j(\omega t + \varphi_1)] \tag{27b}$$

$$\overline{i_2^2} = 2eI_2\Delta f, \qquad \overline{i_3^2} = 2eI_3\Delta f, \qquad \overline{i_4^2} = 2eI_4\Delta f \tag{28}$$

For the case where $\alpha/\alpha_0 \approx 1$ and at moderate frequencies, both noise generators i_1' and i_1'' can be combined to give one

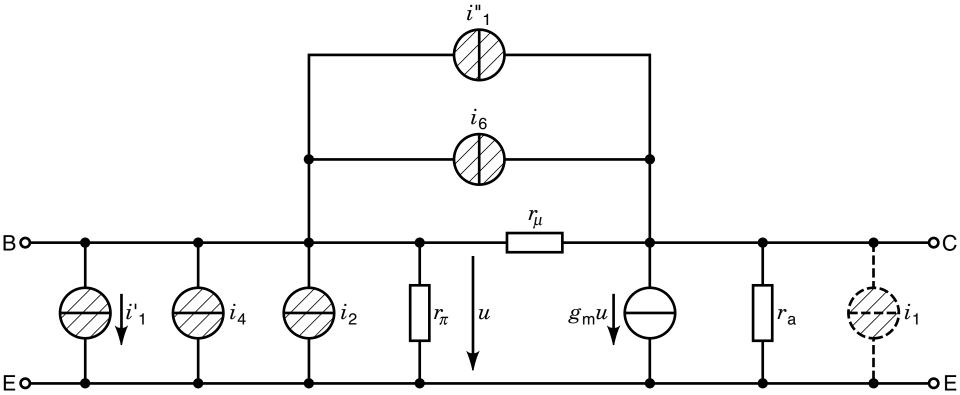

Figure 9. Noise equivalent circuit for a BJT including shot-noise generators for all current components (cf. Fig. 8).

noise source i_1 located between the collector and emitter (see Fig. 9), representing pure shot noise:

$$\overline{i_1^2} = 2eI_1\Delta f \tag{29}$$

Thermal noise sources due to parasitic resistances can be included as described in the next section.

RF-Noise Model of an InP/InGaAs HBT

Figure 10 shows a small-signal equivalent circuit including the noise sources for the simultaneous modeling of s parameters and noise behavior applied to an InP/InGaAs HBT (36). Referring to the preceding section the shot-noise generators of the input and the output of the intrinsic transistor can be found as

$$\overline{i_{\rm nB}^2} = 2eI_{\rm Bn} \tag{30a}$$

with $I_{\rm Bn}$ the noise model value of the input,

$$\overline{i_{\rm nC}^2} = 2eI_{\rm Cn} \tag{30b}$$

with $I_{\rm Cn}$ the noise model value of the output,

$$\overline{i_{\rm nB}^* i_{\rm nC}} = \underline{C}\sqrt{i_{\rm nB}^2 i_{\rm nC}^2} \tag{30c}$$

with $\underline{C} = C_R + jC_I$ the cross-correlation coefficient.

The thermal noise of the resistances $R_{\rm BB}$, $R_{\rm CC}$, and $R_{\rm EE}$ (cf. Fig. 10) are represented by three uncorrelated noise current sources ($i_{\rm nBB}$, $i_{\rm nCC}$, $i_{\rm nEE}$). For noise modeling, the equivalent noise temperatures $T_{\rm B}$, $T_{\rm C}$, and $T_{\rm E}$ of the resistances and the model parameter values $I_{\rm Bn}$, $I_{\rm Cn}$, and $\underline{C}$ have to be extracted. The parasitics due to the pads are considered by the extrinsic elements $L_{\rm B}$, $L_{\rm C}$, and $L_{\rm E}$ as well as $C_{\rm pBE}$, $C_{\rm pCE}$, and $C_{\rm pBC}$.

Experimental Results and Verification of the Model for an InAlAs/InGaAs/InP HFET

As an example of the applicability of the presented noise models, the RF-noise behavior of a typical InAlAs/InGaAs/InP HFET is presented with a gate length of $L_{\rm G} = 0.7$ μm and a gate width $W_{\rm G} = 80$ μm, which is suitable for millimeter-wave and optoelectronic applications. The material system has been selected to demonstrate the significance of both the impact ionization in the InGaAs channel and the gate-leakage current. In contrast, typical GaAs-based HFETs do not significantly suffer from these phenomena, mainly due to the larger band gap of the corresponding materials (37,38).

All model parameters—the small-signal equivalent elements, equivalent noise temperatures ($T_{\rm P}$, $T_{\rm G}$, and $T_{\rm D}$), and equivalent impact ionization noise current ($i_{\rm im}$)—have been extracted using an optimization algorithm based on the *simulated evolution* (evolution theory and genetic algorithms) (39–43). These optimization strategies have to be applied because an analytical extraction of the model parameters from measured data (s and noise parameters) is impossible due to the large number of model parameters and the complexity of the model.

RF Performance. Figures 11 and 12 show both the measured and the modeled RF data, respectively, in the frequency range from 45 MHz up to 40 GHz. The good agreement demonstrates the applicability of the presented small-signal equivalent circuit including the significant effects of gate leakage and the impact-ionization phenomena. If these particular elements are neglected the resulting calculations demonstrate a significant deviation especially for s_{21} and s_{22} at lower frequencies as depicted by the dashed lines in Fig. 11. The modeled parameters are calculated from the small-signal equivalent circuit, extracted from RF measurements using

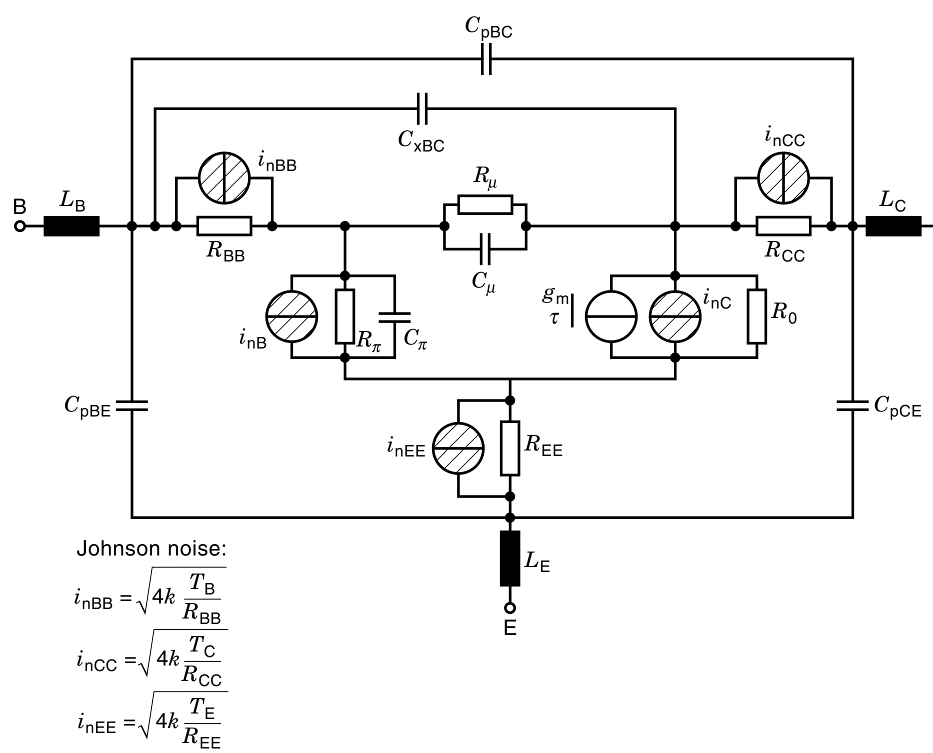

Figure 10. Small-signal and noise equivalent circuit of an HBT.

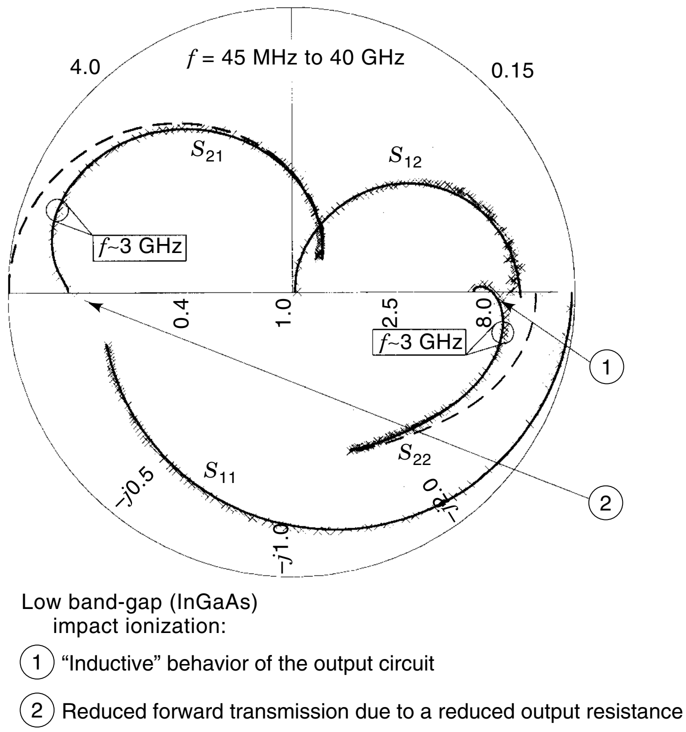

Figure 11. Measured (×) and modeled (—) scattering parameters versus frequency of an InAlAs/InGaAs/InP HFET at a bias condition at which impact ionization occurs (T = 300 K, V_{DS} = 1.5 V, V_{GS} = 0 V, L_G = 0.7 μm, W_G = 80 μm). Note: Dashed lines (––) represent modeled scattering parameters versus frequency if impact ionization is neglected.

Table 1. Bias Condition, Geometry, Performance Data, and the Extracted Small-Signal Equivalent Elements of InAlAs/InGaAs/InP HFET

Bias Condition		Gate Geometry
V_{DS} = 1.5 V	V_{GS} = 0 V	L_G = 0.7 μm
I_D = 31.8 mA	I_G = −18 μA	W_G = 80 μm
Cutoff Frequencies		
f_T = 45 GHz	f_{max} = 152 GHz	
Small-Signal Equivalent Elements		
C_{in} = 14.2 fG	C_{io} = 4 fF	C_{out} = 28.2 fF
R_G = 3 Ω	L_G = 63.1 pH	C_{GS} = 210.5 fF
R_S = 8 Ω	L_S = 3.8 pH	L_D = 152 pH
R_{GS} = 2.8 Ω	R_{DS} = 420 Ω	R_{PGS} = 12 kΩ
R_D = 10 Ω	C_{DS} = 8.2 fF	R_{PGD} = 70.7 kΩ
C_{GD} = 9.5 fF	g_m = 69 mS	τ = 0.22 ps
R_{im} = 38 kΩ	C_{im} = 1.42 fF	$g_{m,im}$ = 4.26 mS

the previously described *simulated evolution.* The corresponding bias condition, geometry, and performance data, as well as the extracted small-signal equivalent elements, are listed in Table 1.

Figure 13 shows the typical bias-dependent behavior of the extracted transconductance $g_{m,im}$ at room temperature (T = 300 K). The low transconductance $g_{m,im}$ for small drain–source voltages V_{DS} demonstrates the negligible influence of impact ionization on the RF performance at low V_{DS} corresponding to low fields in the HFET channel. With increasing V_{DS}, impact ionization and inductive behavior of s_{22} occur, correlated with a drastically increased transconductance $g_{m,im}$.

Noise Behavior. The measured and modeled noise parameters (F_{min}, R_n, g_n, G_{assoc}, and $\underline{\Gamma}_{opt}$) of the HFET are shown in Fig. 14. Because of the Lorentzian shape of the external short-circuit noise current $i_{im,ext}$ [cf. Eq. (25)], corresponding to an upper frequency band limitation especially at low frequencies, a strong impact on the noise performance can be observed. The phenomenon of impact ionization now leads to an increase in the minimum noise figure F_{min}. Especially the increase in the minimum noise figure at low frequencies reflects the influence of the impact-ionization process. In contrast to the influence of a gate-leakage current (33), impact ionization leads to higher optimum generator impedances and causes a

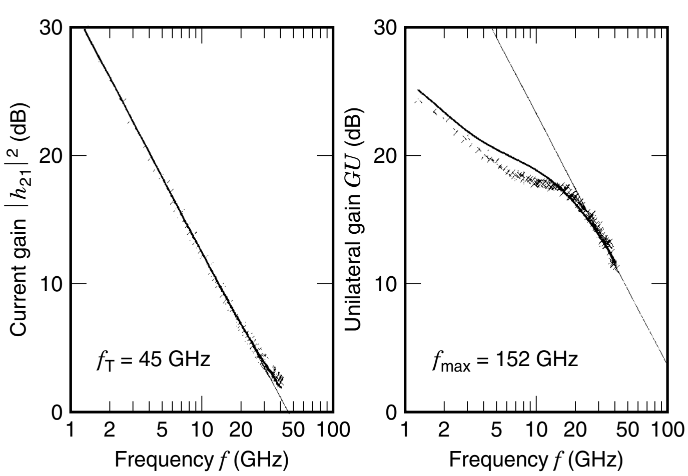

Figure 12. Measured (×) and modeled (—) current gain $|h_{21}|^2$ and unilateral gain G_U versus frequency of an InAlAs/InGaAs/InP HFET at a bias condition at which impact ionization occurs (T = 300 K, V_{DS} = 1.5 V, V_{GS} = 0 V, L_G = 0.7 μm, W_G = 80 μm).

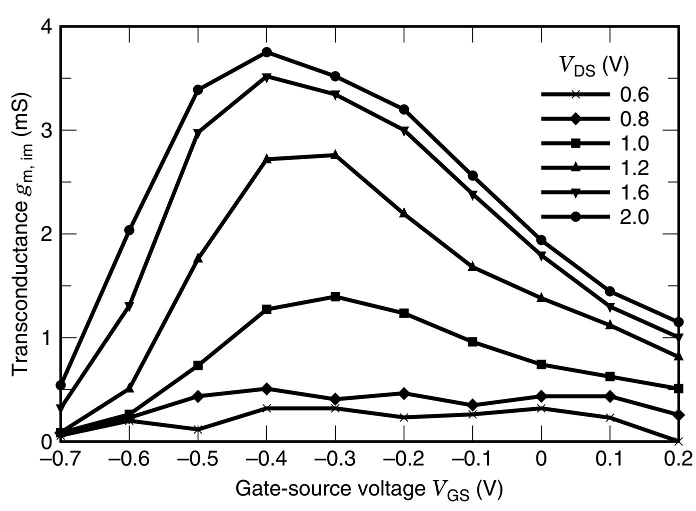

Figure 13. Impact-ionization transconductance $g_{m,im}$ versus the gate–source voltage V_{GS}, with the drain-source voltage V_{DS} as a parameter (L_G = 0.15 μm, W_G = 100 μm, T = 300 K).

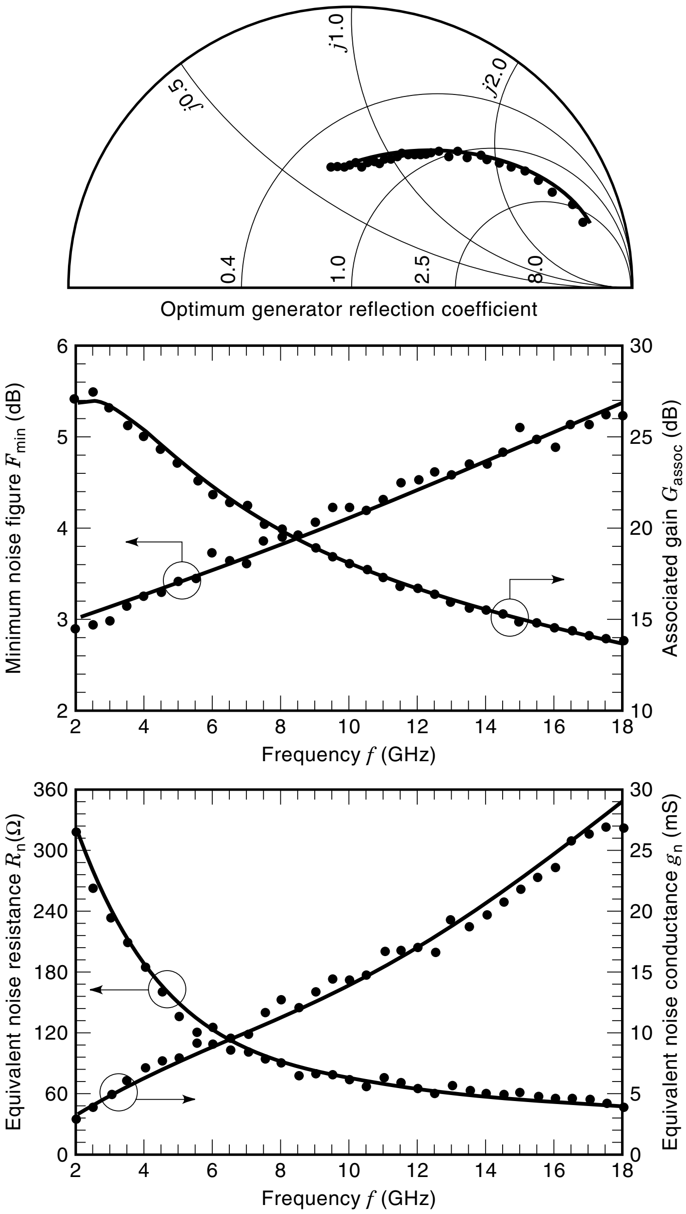

Figure 14. Measured (●) and modeled (—) noise parameters versus frequency of an InAlAs/InGaAs/InP HFET at a bias condition at which impact ionization occurs (V_{DS} = 1.5 V, V_{GS} = 0 V, I_D = 31.8 mA, L_G = 0.7 μm, W_G = 80 μm, $T = T_a$ = 300 K).

large increase of the equivalent noise resistance R_n at low frequencies as well. The inductive behavior of the output path of the HFET also affects the associated gain G_{assoc} and leads to a decrease at low frequencies. The three equivalent noise temperatures (T_G, T_P, and T_D) and the equivalent impact ionization noise current i_{im} of the modeled extrinsic noise parameters are listed in Table 2.

Intrinsic Equivalent Noise Sources. The intrinsic equivalent noise sources (44) of the HFET are strongly bias dependent (32). Figure 15 shows the drastic increase in the extracted impact-ionization noise current i_{im} with higher drain–source voltages V_{DS}, while at low drain-source voltages (V_{DS} < 0.7 V) this component is negligible. In the latter case electron energies are smaller than the band gap and are insufficient to generate electron–hole pairs. With increasing drain–source voltage ($>V_{DS} \approx 0.8$ V) impact ionization occurs and leads to additional noise currents that dominate the noise behavior of the transistor. This behavior reflects the strong correlation between impact ionization, the bias condition, and the generated total noise current. Due to the fact that the level of the extracted impact-ionization noise current i_{im} exceeds the equivalent shot-noise drain current ($i_D = \sqrt{2eI_D}$) in a wide range of bias conditions, carrier multiplication (6,30,31) should occur in the high-field domain, leading to the following relation:

$$i_{int} \propto f(M(E))\sqrt{2eI_D} \tag{31}$$

where $f(M(E))$ reflects the dependence of the multiplication factor $M(E)$ on the electric field strength (30). The relation between the multiplication factor $M(E)$ and the majority-carrier impact-ionization rate per unit length, $\alpha(x, E)$, can be described according to (30)

$$M(E) = \exp\left(\int_0^{L_{eff}} \alpha(\xi, E)\, d\xi\right) \tag{32}$$

with L_{eff} the effective length of the impact-ionization region.

Because of the position-dependent electric field strength and impact-ionization rate, no simple analytical expression

Table 2. Extracted Equivalent Noise Temperatures and Noise Current of the Modeled HFET (V_{DS} = 1.5 V, V_{GS} = 0 V, I_D = 31.8 mA, L_G = 0.7 mm, W_G = 80 mm, $T = T_a$ = 300 K)

Equivalent channel noise temperature
T_G = 4014.9 K
Equivalent output noise temperature
T_D = 18,007.84 K
Equivalent gate-leakage noise temperature
T_P = 918.65 K
Equivalent impact ionization noise current
i_{im} = 146 pA

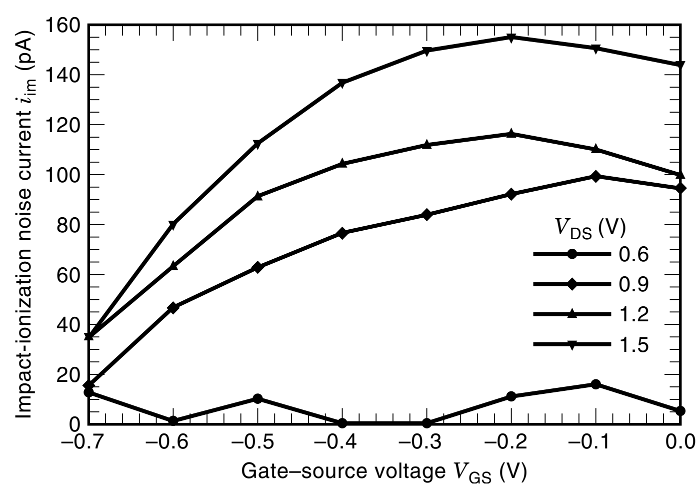

Figure 15. Extracted equivalent intrinsic impact-ionization noise current i_{im} versus the gate–source voltage V_{GS} with drain–source voltage V_{DS} as a parameter.

can be derived for the relation between bias conditions and the generated impact-ionization noise current i_{im}.

The other equivalent intrinsic noise sources show the expected bias dependence (44) and reflect the strong correlation between the equivalent intrinsic noise sources (i_{D}, i_{P}, and v_{G}) and the physical noise sources, such as shot-noise drain current i_{sD} [Eq. (33)] and shot-noise gate current i_{sG} [Eq. (34)]:

$$i_{\mathrm{sD}} = \sqrt{2eI_{\mathrm{D}}} \tag{33}$$

$$i_{\mathrm{sG}} = \sqrt{2eI_{\mathrm{G}}} \tag{34}$$

The equivalent output noise current i_{D} that is dependent on the gate–source voltage V_{GS} versus the shot-noise drain current is shown in Fig. 16. The equivalent noise current i_{D} is dominated by a reduced shot-noise drain current (28). The corresponding correlation is given by

$$i_{\mathrm{D}} = \sqrt{4k\frac{T_{\mathrm{D}}}{R_{\mathrm{DS}}}} \cong k_{\mathrm{D}}\sqrt{2eI_{\mathrm{D}}} + i_{\mathrm{D0}} \tag{35}$$

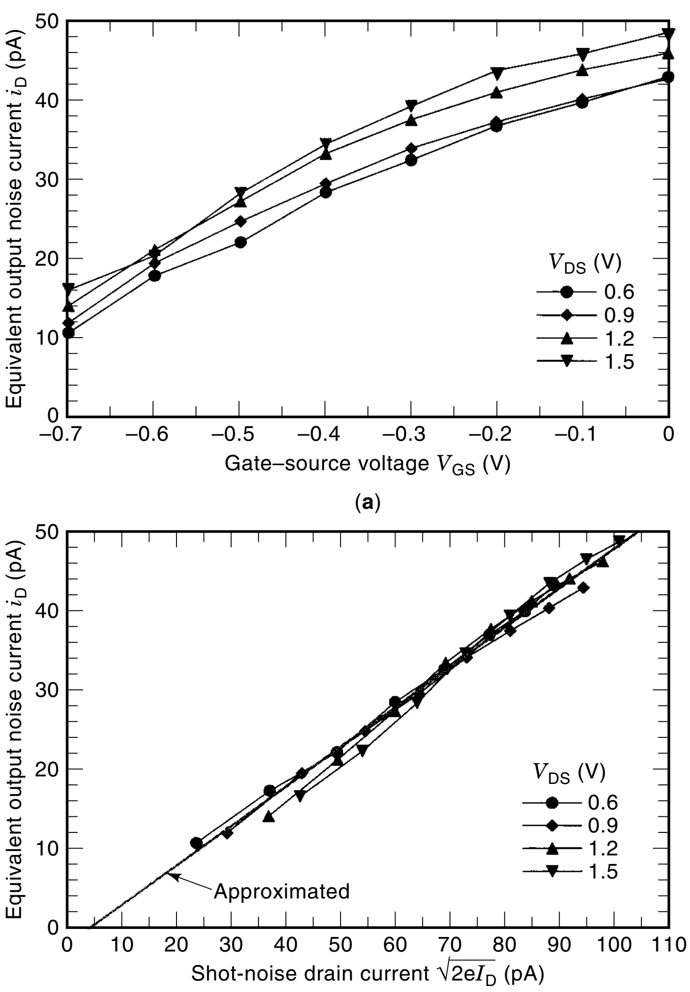

Figure 16. Extracted equivalent output noise current i_{D} versus (a) gate–source voltage V_{GS} and (b) the shot noise drain current with drain–source voltage V_{DS} as a parameter.

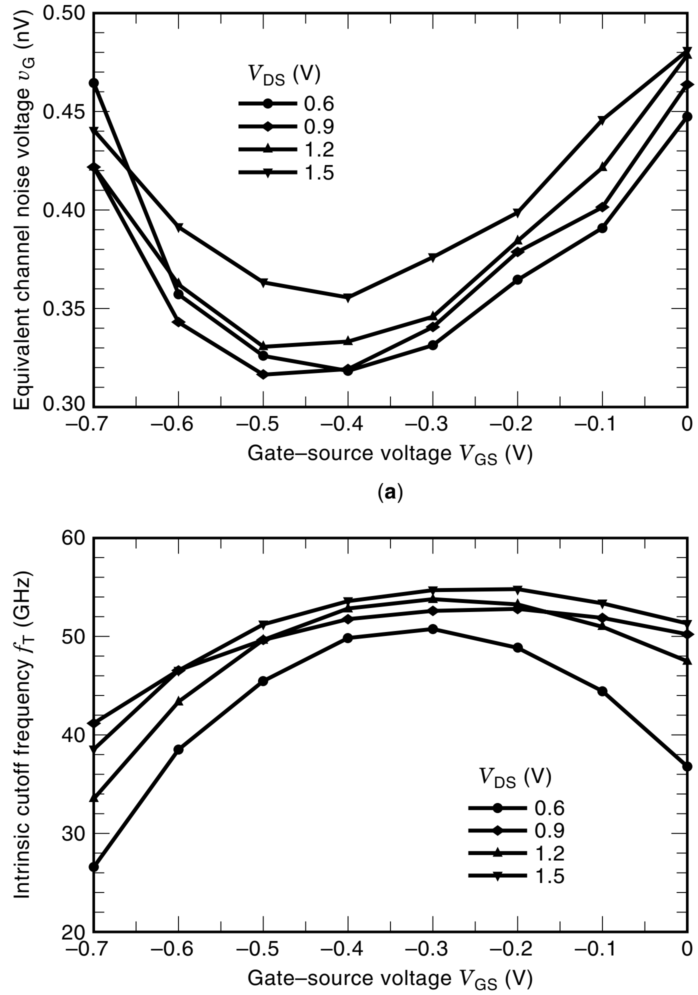

Figure 17. (a) Equivalent channel noise voltage v_{G} and (b) intrinsic current gain cutoff frequency f_{T} (below) versus the gate–source voltage V_{GS} with the drain–source voltage V_{DS} as a parameter.

with

$$k_{\mathrm{D}}, i_{\mathrm{D0}} = \text{const (the value depends on the particular device)} \tag{36}$$

The behavior of the equivalent channel noise voltage v_{G} (Fig. 17) that is dependent on the gate–source voltage V_{GS} exhibits an inversely proportional behavior to the intrinsic current gain cutoff frequency f_T ($f_{\mathrm{T}} = g_{\mathrm{m}}/[2\pi(C_{\mathrm{GS}} + C_{\mathrm{GD}})]$). This is caused by a strong correlation of v_{G} to the intrinsic delay time behavior of the HFET. A transformation of the equivalent channel noise voltage v_{G}, which is a characteristic value for the input circuit of the transistor, to a noise measure of the output circuit can be derived by multiplying v_{G} by the ratio of the square of the transconductance g_{m} and the intrinsic current gain cutoff frequency f_{T}. The transformed channel noise voltage exhibits nearly proportional behavior to the shot-noise drain current (see Fig. 18). Using this transformation the equivalent channel noise voltage v_{G} can be expressed by

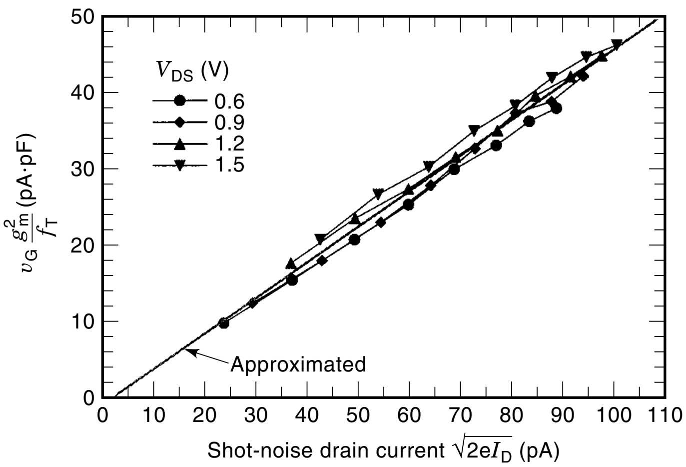

Figure 18. Extracted transformed equivalent channel noise voltage versus the shot-noise–drain current with the drain–source voltage V_{DS} as parameter, respectively.

the following linear approximation:

$$v_G \frac{g_m^2}{f_T} = \sqrt{4kT_G R_{GS}}\, \frac{g_m^2}{f_T} \cong k_G \sqrt{2eI_D} + i_{D1} \tag{37}$$

where

$$k_G, i_{D1} = \text{const (the value depends on the particular device)} \tag{38}$$

Figure 19 shows the equivalent gate-leakage noise current i_P in dependence on the gate–source voltage V_{GS} and versus the shot-noise gate current. The equivalent gate-leakage noise current i_P is nearly proportional to the shot-noise gate current. This clearly demonstrates that a gate tunneling current causes pure shot noise [Eq. (34)] (44). The described behavior leads to

$$i_P = \sqrt{4k\frac{T_P}{R_{PGS}}} \cong \sqrt{2eI_G} \tag{39}$$

These dependencies demonstrate the capability of the presented noise model to separate the intrinsic noise sources, and the correlation to physical noise processes. Furthermore, only two independent noise parameter measurements are sufficient to extract the unknown parameters (k_G, k_D, i_{D0}, i_{D1}) in Eqs. (35) to (38).

With the extracted bias dependence of the small-signal equivalent elements and using Eqs. (35) to (39), the behavior of the channel noise voltage v_G, and output noise current i_D as well as the equivalent gate-leakage noise current i_P of HFETs can be derived for each bias condition at any frequency where $1/f$ noise is negligible.

EXTENSION AND APPLICATION OF PRESENTED NOISE MODELS

Analytical and Scaleable Noise Model for the HFET

In the case where the influence of impact ionization and gate-leakage current on the small-signal and noise performance can be neglected, the RF noise of the HFET is mainly dominated by channel and output noise sources [cf. Eqs. (35) and (37)].

The parameters k_G and k_D are bias independent, but gate-geometry dependent. To investigate the geometry dependence (gate length L_G and gate width W_G) of these parameters, the equivalent intrinsic noise sources of transistors with varying gate width and gate length have been extracted and analyzed and are dependent on the shot-noise drain current (Fig. 20). Based on these investigations the following final analytical expressions can be derived for the intrinsic equivalent noise sources (45):

$$i_{D,n} = \sqrt{4k\frac{T_D}{R_{DS}}} \cong K_D(\sqrt{2e|I_D|} - \sqrt{2eI_{D,d}}) \tag{40}$$

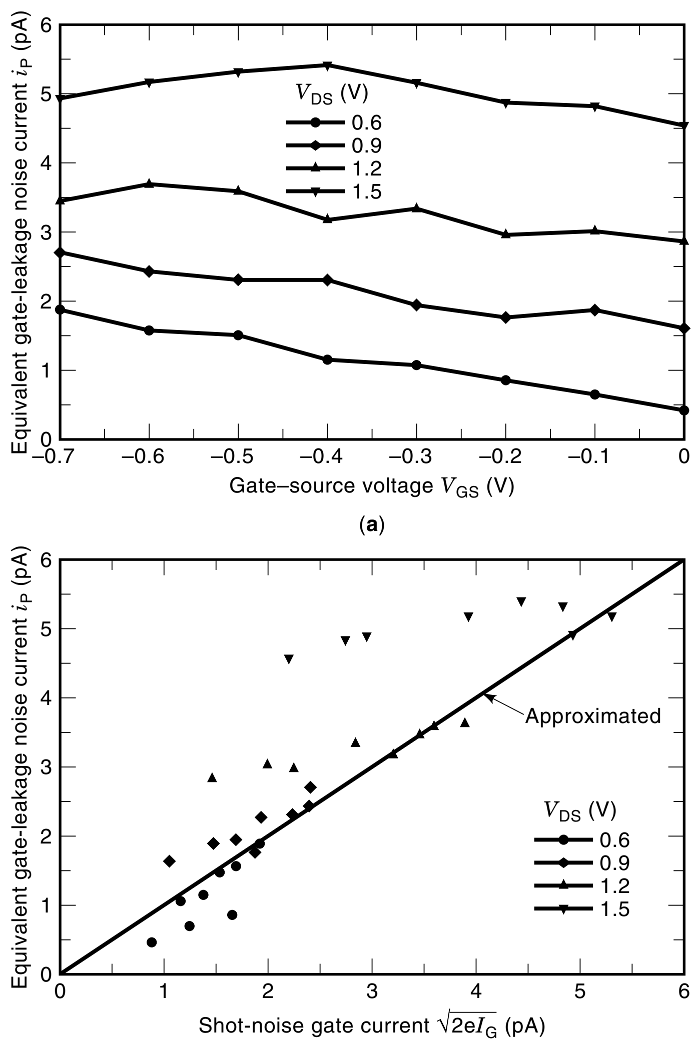

Figure 19. Extracted equivalent gate-leakage noise current i_P versus (a) the gate–source voltage V_{GS} and (b) shot-noise gate current with the drain–source voltage V_{DS} as a parameter.

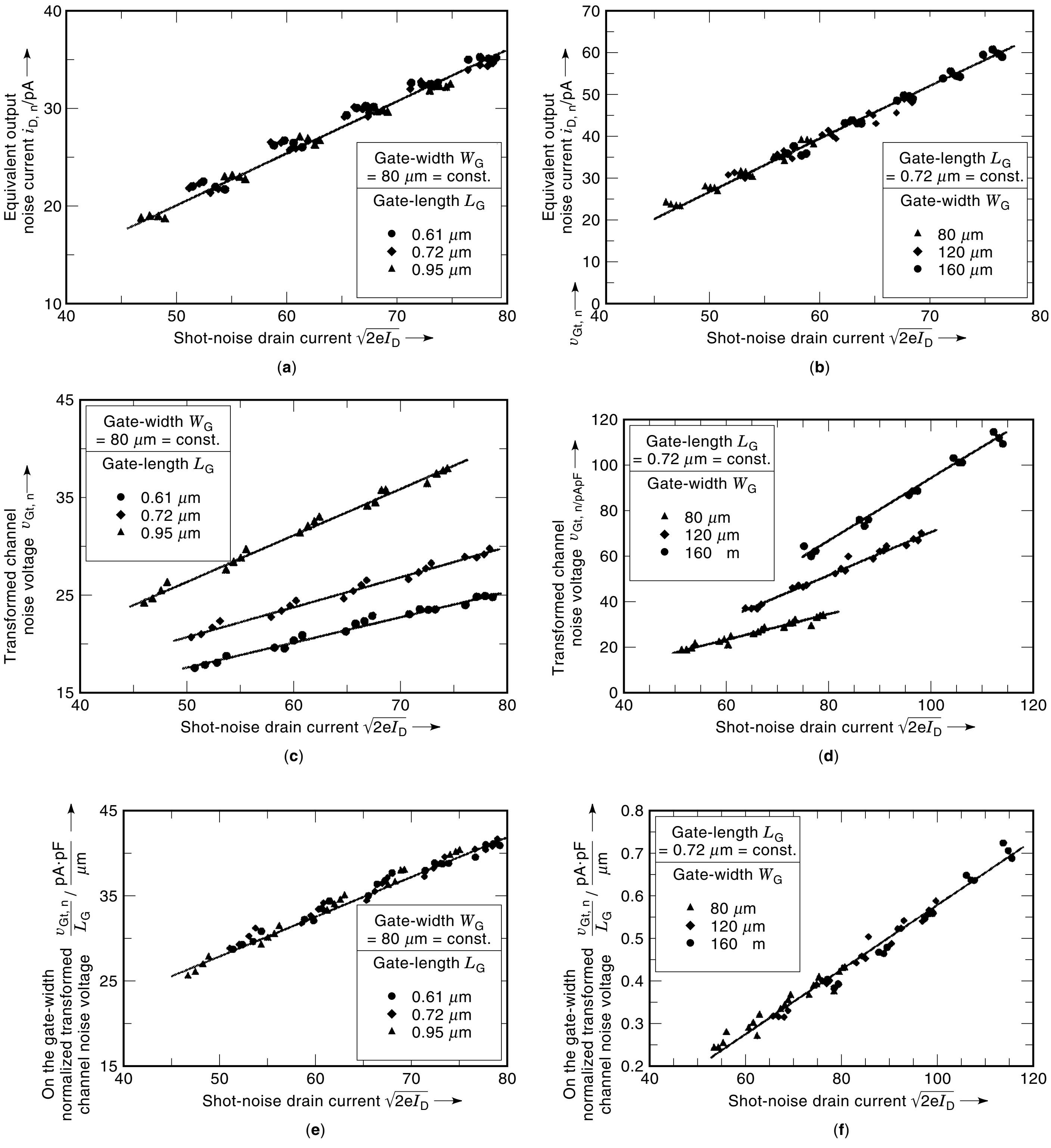

Figure 20. (a,b) Equivalent output noise current $i_{D,n}$ versus the shot-noise drain current with (a) gate-length L_G as a parameter and (b) gate-width W_G as a parameter. (c,d) Transformed equivalent channel noise voltage $v_{Gt,n}$ versus the shot-noise drain current with (c) gate-length L_G as a parameter and (d) gate-width W_G as a parameter. (e,f) Normalized transformed equivalent channel noise voltage $v_{Gt,n}$ versus the shot-noise drain current (e) normalized on the gate-length L_G and (f) normalized on the gate-width W_G (T = 300 K, V_{DS} = 0.9 V up to 1.8 V, V_{GS} = −0.3 V up to 0.1 V).

Table 3. Scaling Properties of Some Small-Signal Equivalent Elements and Device Parameters

Gate-Length Dependence	Gate-Width Dependence
$g_m \neq f(L_G) = \text{const}$	$g_m \propto W_G$
$C_{GS} \propto L_G$	$C_{GS} \propto W_G$
$f_T \propto 1/L_G$	$f_T \neq f(W_G) = \text{const}$
$I_D \neq f(L_G) = \text{const.}$	$I_D \propto W_G$

and

$$v_{\mathrm{G,n}} = \sqrt{4kT_{\mathrm{G}}R_{\mathrm{GS}}} \cong \frac{K_{\mathrm{G}}W_{\mathrm{G}}L_{\mathrm{G}}f_{\mathrm{T}}}{g_{\mathrm{m}}^2}(\sqrt{2e|I_{\mathrm{D}}|} - \sqrt{2eI_{\mathrm{D,g}}}) \tag{41}$$

where K_D and K_G are only material dependent parameters (bias and gate-geometry independent). In practice, the small influence of the parameters $I_{D,d}$ and $I_{D,g}$ can be neglected, so that the following equations are sufficient for the prediction of the noise behavior:

$$i_{\mathrm{D,n}} = \sqrt{4k\frac{T_{\mathrm{D}}}{R_{\mathrm{DS}}}} \cong K_{\mathrm{D}}\sqrt{2e|I_{\mathrm{D}}|} \tag{42}$$

and

$$v_{\mathrm{G,n}} = \sqrt{4kT_{\mathrm{G}}R_{\mathrm{GS}}} \cong K_{\mathrm{G}}W_{\mathrm{G}}L_{\mathrm{G}}\sqrt{2e|I_{\mathrm{D}}|}\,\frac{f_{\mathrm{T}}}{g_{\mathrm{m}}^2} \tag{43}$$

A simplified intrinsic temperature noise model (46) is used to derive analytical expressions for all four noise parameters:

$$F_{\min} = 1 + \frac{2}{T_0}\frac{f}{f_{\mathrm{T}}}\sqrt{R_{\mathrm{GS}}T_{\mathrm{G}}\frac{T_{\mathrm{D}}}{R_{\mathrm{DS}}}} \tag{44}$$

$$R_{\mathrm{S,opt}} = \frac{f_{\mathrm{T}}}{f}\sqrt{R_{\mathrm{GS}}T_{\mathrm{G}}\frac{R_{\mathrm{DS}}}{T_{\mathrm{D}}}} \tag{45}$$

$$X_{\mathrm{S,opt}} = \frac{1}{f}\frac{1}{2\pi C_{\mathrm{GS}}} \tag{46}$$

and

$$R_{\mathrm{n}} = \frac{1}{T_0}\left(R_{\mathrm{GS}}T_{\mathrm{G}} + \frac{T_{\mathrm{D}}}{R_{\mathrm{DS}}}\frac{1}{g_{\mathrm{m}}^2}\right) \tag{47}$$

These estimates are sufficient for the geometry scaling of the intrinsic noise parameters of HFETs. Using these formulas and Eq. (42) and (43) a correspondence between the intrinsic noise parameters and additional transistor parameters can be derived:

$$F_{\min} - 1 = \frac{f}{T_0}\frac{K_{\mathrm{G}}K_{\mathrm{D}}}{2k}W_{\mathrm{G}}L_{\mathrm{G}}\frac{2e|I_{\mathrm{D}}|}{g_{\mathrm{m}}^2} \tag{48}$$

$$R_{\mathrm{S,opt}} = \frac{f_{\mathrm{T}}}{f}\frac{K_{\mathrm{G}}}{K_{\mathrm{D}}}W_{\mathrm{G}}L_{\mathrm{G}}\frac{f_{\mathrm{T}}}{g_{\mathrm{m}}^2} \tag{49}$$

$$X_{\mathrm{S,opt}} = \frac{1}{f}\frac{1}{2\pi C_{\mathrm{GS}}} \tag{50}$$

and

$$R_{\mathrm{n}} = \frac{1}{T_0}\frac{2e|I_{\mathrm{D}}|}{4kg_{\mathrm{m}}^2}\left[\left(K_{\mathrm{G}}W_{\mathrm{G}}L_{\mathrm{G}}\frac{f_{\mathrm{T}}}{g_{\mathrm{m}}^2}\right)^2 + K_{\mathrm{D}}^2\right] \tag{51}$$

With these estimates for the gate-length and gate-width dependences the behavior of the drain current I_D, the transconductance g_m and the gate–source capacitance C_{GS} (Table 3), as well as the geometry dependence of the intrinsic noise parameters can be obtained (Table 4).

Table 4. Derived Scaling Behavior of the Intrinsic Noise Parameters

Gate-Length Dependence	Gate-Width Dependence
$F_{\min} - 1 \propto L_G$	$F_{\min} - 1 \neq f(W_G) = \text{const}$
$R_{Q,\text{opt}} \propto 1/L_G$	$R_{Q,\text{opt}} \propto 1/W_G$
$X_{Q,\text{opt}} \propto 1/L_G$	$X_{Q,\text{opt}} \propto 1/W_G$
$R_n \neq f(L_G) = \text{const}$	$R_n \propto 1/W_G$

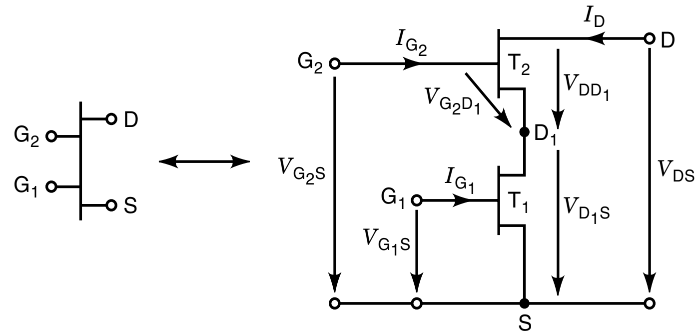

Figure 21. Dual-gate HFET and its equivalent circuit using two HFETs and the definition of extrinsic and intrinsic voltages and currents.

Dual-Gate HFET in Cascode Configuration

Figure 21 shows a dual-gate HFET (DGHFET) and the corresponding equivalent circuit with the definition of extrinsic

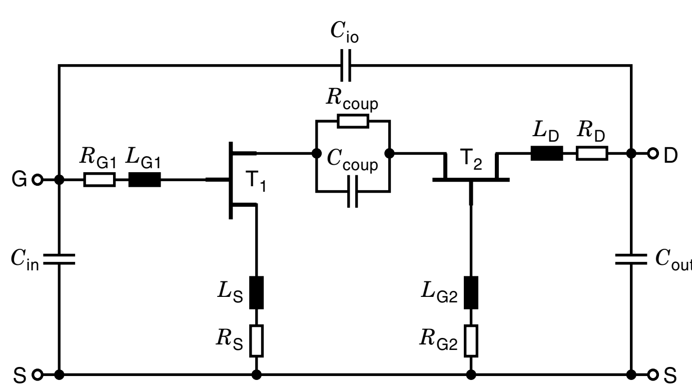

Figure 22. Small-signal equivalent circuit for a DGHFET in cascode configuration.

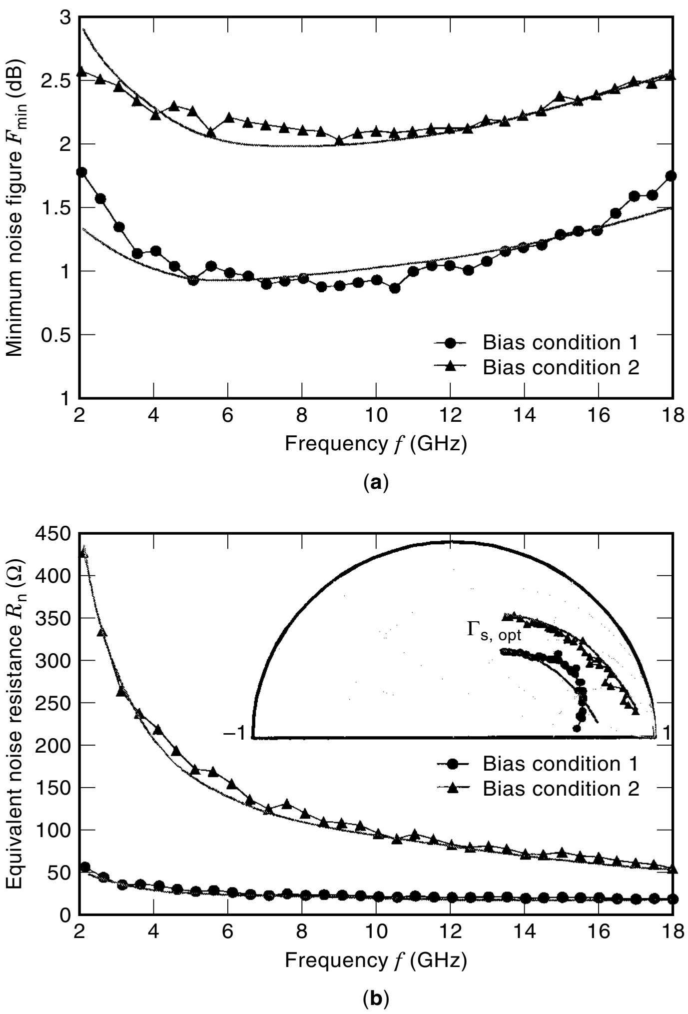

Figure 23. Measured and modeled noise parameter for (a) bias conditions 1 (V_{DS} = 3 V, V_{G_1S} = 0.1 V, V_{G_2S} = 0.6 V) and (b) bias conditions 2 (V_{DS} = 3 V, V_{G_1S} = 0 V, V_{G_2S} = 2.2 V).

and intrinsic voltages and currents (47). The DGHFET can be represented by two single-gate HFETs (SGHFETs), which are connected at the virtual node D_1 (48). Consequently, the DGHFET can be separated into three parts (Fig. 22):

- The parasitic environment
- One single-gate HFET in a common-source configuration
- One single-gate HFET in a common-gate configuration

All parts are connected by a coupling network consisting of an additional resistance R_{coup} and a capacitance C_{coup}.

Correspondingly, the DGHFET can be modeled on the particular equivalent circuits of the SGHFET, described in the section on InAlAs/InGaAs/InP HFETs. The small-signal equivalent elements as well as the noise temperatures and currents can also be extracted using the evolutionary algorithm (39).

Measured and modeled noise properties of a typical InP-based DGHFET are shown in Fig. 23 at two bias conditions, indicated in Table 5, with a comparable drain current. The modeled equivalent noise temperatures, the corresponding resistances, and the extracted data of the noise sources (Table 5) demonstrate the influence of impact ionization dependence on the bias condition.

Compared to the single-gate HFET, the dual-gate HFET shows a reduced impact-ionization noise component at comparable bias conditions (49). Additionally, the RF performance of the DGHFET corresponds to that of the SGHFET. Moreover, even an increase of the unilateral gain and a reduced feedback can be obtained. Due to this fact, dual-gate HFETs are commonly used for mixers, oscillators, variable gain amplifiers, and high-frequency applications such as OEICs (optoelectronic integrated circuits) or MMIC (monolithic microwave integrated circuit) amplifiers (50).

Application of Noise Models for Circuit Design

The importance of reliable noise modeling of single devices shall be demonstrated for an optoelectronic receiver circuit. The necessary minimum optical input power $P_{opt,min}$ applied to an optoelectronic receiver in order to detect the original signal tolerating a certain error can be derived as (51)

$$P_{\mathrm{opt,min}} = \frac{\hbar c_0}{\eta e \lambda} Q \sqrt{\overline{i_{\mathrm{na}}^2}} \tag{52}$$

where $\hbar$ is Planck's constant, c_0 the light velocity, η the quantum efficiency, λ the wavelength of the light, Q the noise factor, which is $Q \approx 6$ for a bit error rate of 10^{-9} and $\sqrt{\overline{i_{\mathrm{na}}^2}}$ the root mean square of the equivalent input noise current density of the electrical amplifier.

The noise factor Q is derived from probability calculations that consider the stochastical nature of the noise signal as well as the pseudorandom characteristic of a real information signal. Q can be derived from the following Gaussian probability integral, where BER is the bit error rate of the detected digital signal behind the decision circuit:

$$\mathrm{BER} = \frac{1}{2\pi} \int_Q^{\infty} e^{-x^2/2}\, dx \tag{53}$$

Typically, a bit error rate of 10^{-9} is assumed to be the maximum tolerable number of incorrectly detected bits per second. Hence, the corresponding noise factor equals $Q \approx 6|_{\mathrm{BER}=10^{-9}}$.

Table 5. Modeled Intrinsic Temperatures and Resistances Describing the Noise Behavior of the DGHFET

Bias Condition 1	Bias Condition 2
$V_{DS} = 3$ V, $V_{G_1S} = 0.1$ V, $V_{G_2S} = 0.6$ V	$V_{DS} = 3$ V, $V_{G_1S} = 0$ V, $V_{G_2S} = 2.2$ V
$T_{G_1} = 39215$ K, $R_{GS_1} = 2.9\ \Omega$	$T_{G_1} = 5323$ K, $R_{GS_1} = 0.98\ \Omega$
$T_{P_1} = 587$ K, $R_{PGS_1} = 3.9 \times 10^5\ \Omega$	$T_{P_1} = 12337$ K, $R_{PGS_1} = 6.3 \times 10^5\ \Omega$
$T_{D_1} = 6349$ K, $R_{DS_1} = 149.5\ \Omega$	$T_{D_1} = 38272$ K, $R_{DS_1} = 233.6\ \Omega$
$i_{im_1} = 98$ pA	$i_{im_1} = 496$ pA
$T_{G_2} = 5061$ K, $R_{GS_2} = 0.57\ \Omega$	$T_{G_2} = 4827$ K, $R_{GS_2} = 0.63\ \Omega$
$T_{D_2} = 464$ K, $R_{DS_2} = 84.8\ \Omega$	$T_{D_2} = 300$ K, $R_{DS_2} = 277.8\ \Omega$
$i_{im_2} = 9$ pA	$i_{im_2} = 0$ pA

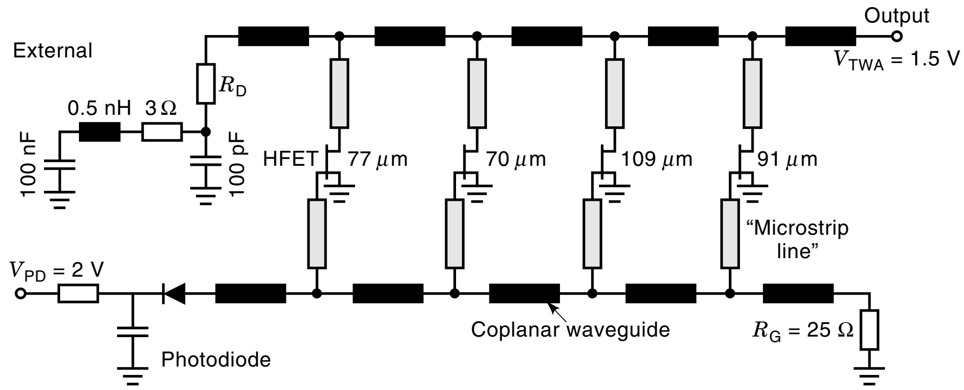

Figure 24. Circuit layout of a four-stage traveling wave amplifier (TWA) combined with a p–i–n photodiode.

The mean input noise current $\sqrt{\overline{i_{na}^2}}$ is a function of numerous device- and circuit-related parameters. In particular the noise sources of the active devices—as discussed in earlier sections—are the dominant contributors at higher frequencies. The second important contribution comes from thermal noise currents generated in ohmic resistors that can be found at different locations of the receiver circuit itself. A closed formulation taking into account some of the small-signal related device parameters was derived in Ref. 51 and can be written as

$$\overline{i_{na}^2} = \frac{4kT}{R_f} X_1 B + 2eI_L X_2 B + \frac{4kT\Gamma}{g_m}(2\pi C_T)^2 (f_c X_f B^2 + X_3 B^3) \tag{54}$$

where X_1, X_2, X_3, and X_f are special weight functions (Personick integrals), B is the bit rate of the data stream, I_L is the total leakage current [a combination of the dark current of the photodetector (PD) and the gate-leakage current of the input transistor), g_m is the transconductance of the first transistor, C_T is the total capacitance (usually $C_T = C_{gs} + C_{PD}$), R_f is the feedback resistance, f_c is the corner frequency of the $1/f$ noise contribution, and Γ is the channel noise factor (a function of transistor-related parameters). In general, the main aim of noise modeling in conjunction with circuit design and development is to enable a reliable estimation of the noise behavior of the total circuit.

As an example for the applicability of the already mentioned temperature noise model (TNM) (see the section entitled "Analytical and Scalable Noise Model for the HFET") for circuit noise simulation, the optoelectronic circuit shown in Fig. 24 is discussed. It consists of a four stage traveling-wave amplifier (TWA) combined with a p–i–n photodiode (PD) to form a high-speed receiver module for transfer rates up to 35 Gbit/s (52,53). The TWA comprises four HFET devices with varying gate widths, hence utilizing the scalability of the applied noise model. The single stages within the TWA are fed from an input transmission line that is connected to the PD (left side) and terminated by a resistor at the end (right side). The single line segments are built up as coplanar waveguides (CPWs), and the feeds toward the transistor gate contact are airbridge interconnections treated like microstrip lines (MSLs) with a permittivity of $\epsilon_r = 1$. At the drain ends, feeding MSL lines are connected to a CPW output transmission line, which again is terminated by a complex impedance (RC combination) at the opposite end of the RF output. Figure 25 shows a photograph of the realized receiver.

The noise contributions of interest are mainly generated by the single HFET devices and the termination resistors. During a circuit simulation carried out using the software package Microwave Design Systems (Hewlett-Packard), the noise behavior of the HFETs was considered using the TNM model. The inset diagram in Fig. 26 depicts the transfer characteristic of the TWA derived from RF measurements up to 45 GHz. In the particular case of optoelectronic receivers, the transimpedance is of major interest and is defined as

$$\underline{Z}_T(f) = \frac{\underline{v}_{out}}{\underline{i}_{in}} = \frac{\underline{v}_{out}}{\underline{i}_{ph}} \tag{55}$$

where $\underline{i}_{ph}$ is the photocurrent of the detector generated by the optical signal.

The transfer characteristic is necessary for calculation of the equivalent input noise current $\sqrt{\overline{i_{na}^2}} = \sqrt{\int i_{na}^2(f)df}$, which is not directly measurable. It has to be derived from measurements of the frequency-dependent noise factor F (or the absolute output noise power) by using the reverse transfer function $\underline{Z}_T^{-1}(f)$ (54).

The validity as well as the reliability of the noise simulation is demonstrated in Fig. 26. Here, the simulated as well as the measured and recalculated frequency-dependent input noise current density $i_{na}(f)$ is depicted. The almost negligible differences between the two curves clearly demonstrate the applicability and validity of the noise models used, even for circuit noise simulations. Finally, these results enable the cir-

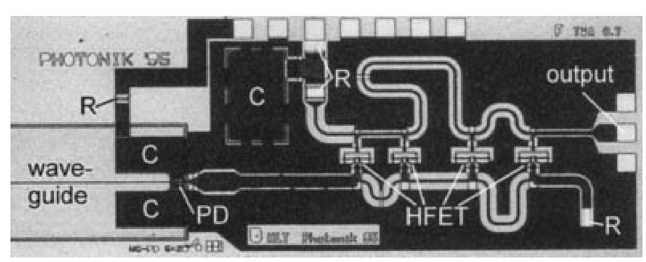

Figure 25. Photograph of realized optoelectronic receiver based on a TWA and waveguide-fed p–i–n photodetector in coplanar technique (C denotes RF-blocking capacitors and R metal-film resistors).

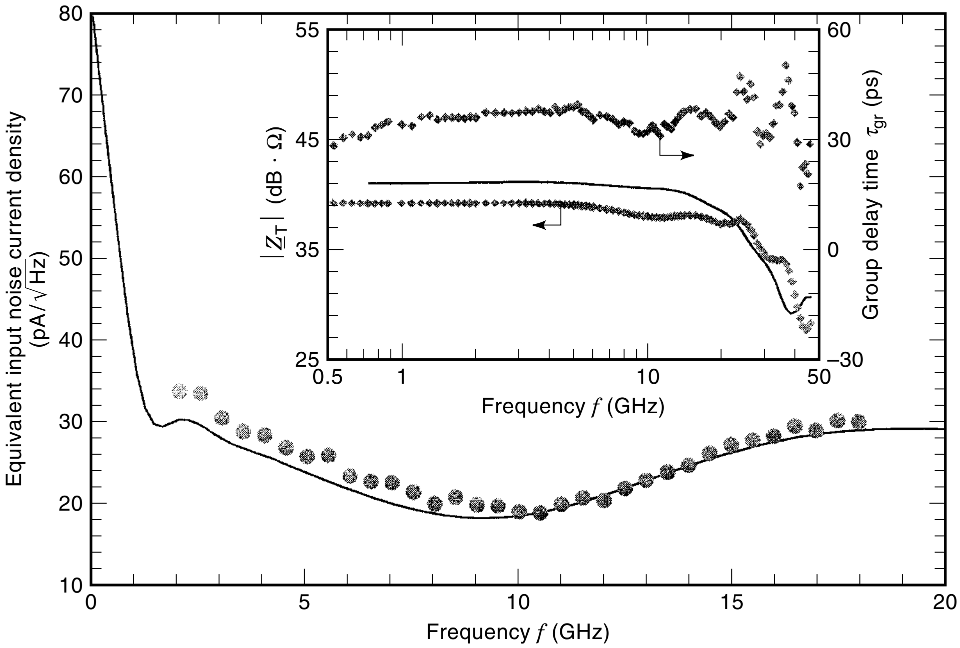

Figure 26. Measured (◆) and modeled (—) transfer characteristic of the TWA (transimpedance $\underline{Z}_T$ versus frequency f). The inset shows the measured (●) and calculated (—) noise data (equivalent input noise current density i_{na} versus frequency f).

cuit designer to achieve reliable estimates of the total receiver sensitivity P_{min} using Eq. (52).

BIBLIOGRAPHY

1. H. Nyquist, Thermal agitation of electric charge in conductors, *Phys. Rev.,* **32**: 110–113, 1928.
2. J. B. Johnson, Thermal agitation of electricity in conductors, *Phys. Rev.,* **32**: 97–107, 1928.
3. H. Bittel and L. Storm, Rauschen, *Eine Einführung zum Verständnis elektrischer Schwankungserscheinungen,* Berlin: Springer-Verlag, 1971.
4. R. Müller, Rauschen, *Halbleiter-Elektronik,* Vol. 15, Berlin: Springer-Verlag, 1979.
5. A. S. Tager, Current fluctuations in a semiconductor (dielectric) under conditions of impact ionization and avalanche breakdown, *Sov. Phys.—Solid State,* **6**: 1919–1925, 1965.
6. R. J. McIntyre, Multiplication noise in uniform avalanche devices, *IEEE Trans. Electron Devices,* **ED-13**: 164–168, 1966.
7. R. J. McIntyre, The distribution of gains in uniformly multiplying avalanche diodes, *IEEE Trans. Electron Devices,* **ED-19**: 703–713, 1972.
8. B. Schiek and H.-J. Siweris, *Rauschen in Hochfrequenzschaltungen,* Heidelberg: Hüthig Buch Verlag, 1990.
9. A. Neidenoff, Lies, *Damm Lies & The Noise Factor (Die falsche Auffassung von der Rauschzahl),* Resumee einer Gegendarstellung zur heutigen Theorie und Praxis, Hochschule für Technik und Wirtschaft des Saarlandes, Saarbrücken, Germany, 1994.
10. D. O. North, The absolute sensitivity of radio receivers, *RCA Rev.,* **6**: 332–343, 1942.
11. H. T. Friis, Discussion on: Noise figures of radio receivers, *Proc. IRE,* **33**: 125ff, 1945.
12. R. Q. Twiss, Nyquist's and Thevenin's theorems generalized for nonreciprocal linear networks, *J. Appl. Phys.,* **26** (5): 599–602, 1955.
13. H. Hillbrand and P. H. Russer, An efficient method for computer aided noise analysis of linear amplifier networks, *IEEE Trans. Circuits Syst.,* **CAS-23**: 235–238, 1976.
14. H. Meschede et al., On-wafer microwave measurement setup for investigations on HEMTs and High T_c superconductors at cryogenic temperatures down to 20 K, *IEEE Trans. Microw. Theory Tech.,* **40**: 2325–2331, 1992.
15. H. Meschede et al., RF investigations on HEMTs at cryogenic temperatures down to 20 K using an on-wafer microwave measurement setup, *Conf. Proc., 22nd Eur. Microw. Conf.,* Helsenki, Finland, 1992, Vol. 1, pp. 151–156.
16. Hewlett-Packard, *Fundamentals of RF and Microwave Noise Figure Measurements,* Hewlett-Packard, Appl. Note 57-1, July 1983.
17. H. Meschede, Hochfrequenzcharakterisierung von Mikrowellentransistoren aus III-V-Halbleitermaterial bei Temperaturen im Bereich von 20 K bis 300 K, Disseration, Universität Duisburg, VDI Verlag, Reihe 21, Elektrotech. No. 144, 1993.
18. ATN Microwave Inc., *Operating Manual NP5B 2-18 GHz Wafer Probe Test Set,* 1993, Billerica, MA.
19. A. Cappy, Noise modeling and measurement techniques, *IEEE Trans. Microw. Theory Tech.,* **36**: 1–10, 1988.
20. E. F. Calandra, G. Martines, and M. Sannino, Characterization of GaAs-FET's in terms of noise, gain and scattering parameters through a noise parameter test set. *IEEE Trans. Microw. Theory Tech.,* **MTT-32**: 231–237, 1984.
21. A. C. Davidson, B. W. Leake, and E. Strid, Accuracy improvements in microwave noise parameter measurements, *IEEE Trans. Microw. Theory Tech.,* **37**: 1973–1978, 1989.
22. J. W. Archer and R. A. Batchelor, Fully automated on-wafer noise characterization of GaAs MESFET's and HEMT's, *IEEE Trans. Microw. Theory Tech.,* **40**: 209–216, 1992.
23. S. M. Sze, *Physics of Semiconductor Devices,* 2nd ed., New York: Wiley, 1981.
24. J.-P. Nougier, Fluctuations and noise of hot carriers in semiconductor materials and devices, *IEEE Trans. Electron Devices,* **41**: 2034–2049, 1994.
25. V. Bareikis et al., Experiments on hot electron noise in semiconductor materials for high-speed devices, *IEEE Trans. Electron Devices,* **41**: 2050–2060, 1994.
26. A. van der Ziel, *Fluctuation Phenomena in Semiconductors,* London: Butterworths, 1959.

27. A. van der Ziel, *Noise in Solid State Devices and Circuits,* New York: Wiley, 1986.
28. J. R. Ragazzini, Noise and random processes, *Proc. IRE,* **50**: 1146–1151, 1962.
29. W. Kleen, Die untere Grenze des Verstärkerrauschens, Physikalische und technische Aspekte, *Phys. Unserer Zeit,* **13** (1): 14–21, 1982.
30. K. M. van Vliet and L. M. Rucker, Theory of carrier multiplication and noise in avalanche devices. Part I: One-carrier processes, *IEEE Trans. Electron Devices,* **ED-26**: 746–751, 1979.
31. K. M. van Vliet, Theory of carrier multiplication and noise in avalanche devices. Part II: Two-carrier processes, *IEEE Trans. Electron Devices,* **ED-26**: 752–764, 1979.
32. R. Reuter et al., Investigation and modeling of impact ionization with regard to the RF- and noise behaviour of HFET, *IEEE Trans. Microw. Theory Tech.,* **45**: 977–983, 1997.
33. R. Reuter, S. van Waasen, and F. J. Tegude, A new noise model of HFET with special emphasis on gate-leakage, *IEEE Electron Device Lett.,* **16** (2): 74–76, 1995.
34. R. Reuter et al., A new RF- and noise model with special emphasis on impact ionization for HFET, *Conf. Proc., Microw. Optron., 9th Exhib. Conf. High Freq. Eng. (MIOP-1997),* Sindelfingen, Germany, 1997, pp. 338–342.
35. R. Reuter et al., On the temperature dependence of the impact ionization in HFET and the corresponding RF- and noise performance, *Conf. Proc., 8th Int. Conf. Indium Phosphide Relat. Mater. (IPRM-1996),* Schwäbisch-Gmünd, Germany, 1996, pp. 654–657.
36. A. Huber et al., RF Noise characterization of a high performance InP/InGaAs HBT, *Conf. Proc., 20th Workshop Compd. Semicond. Devices Integr. Circuits (WOCSDIC-1996),* 1996, Lithuania, pp. 83–84.
37. U. Auer et al., Characterization and analysis of a new gate leakage mechanism at high drain bias in InAlAs/InGaAs heterostructure field-effect transistors, *Conf. Proc., Indium Phosphide Relat. Mater. (IPRM-1996),* Schwäbisch-Gmünd, Germany, 1996, pp. 650–653.
38. U. Auer et al., The impact of pseudomorphic AlAs spacer layers on the gate leakage current of InAlAs/InGaAs heterostructure field-effect transistors, *IEEE Microw. Opt. Technol. Lett.,* **11** (3): 125–128, 1996.
39. M. Agethen et al., A new optimization strategy based on the theory of evolution for the RF-modeling of HFET, *Workshop Proc., Int. IEEE Workshop Experimentally Based FET Device Model. Relat. Nonlinear Circuit Des.,* Kassel, Germany, 1997, pp. 4.1–4.5.
40. M. Agethen et al., Theory of evolution: New optimization strategies for the modeling of HFET-RF-noise-parameters, *Conf. Proc., Microw. Optron., 9th Exhib. Conf. High Freq. Eng. (MIOP-1997),* Sindelfingen, Germany, 1997, pp. 343–347.
41. J. Holland, *Adaptation in Natural and Artificial Systems,* Cambridge, MA: MIT Press, 1992.
42. D. E. Goldberg, *Genetic Algorithms in Search, Optimization, and Machine Learning,* Reading, MA: Addison-Wesley, 1989.
43. Z. Michalewicz, *Genetic Algorithms + Data Structures = Evolution Programs,* Berlin: Springer-Verlag, 1992.
44. R. Reuter et al., A new temperature noise model of HFET with special emphasis on a gate-leakage current and investigation of the bias dependence of the equivalent noise sources, *Conf. Proc., 25th Eur. Microwave Conf.,* Bologna, Italy, 1995, pp. 205–210.
45. R. Reuter and F. J. Tegude, A new analytical and scaleable noise model for HFET, *IEEE Int. Microw. Symp. (MTT-S 1998),* Baltimore, 1998, pp. 137–140.
46. M. W. Pospieszalski, Modeling of noise parameters of MESFET's and MODFET's and their frequency and temperature dependence, *IEEE Trans. Microw. Theory Tech.,* **37**: 1340–1350, 1989.
47. F.-J. Tegude et al., InAlAs/InGaAs/InP Dual-Gate-HFET's: New aspects and properties, *Conf. Proc., 9th Int. Conf. Indium Phosphide Relat. Mater. (IPRM-1997),* Cape Cod, MA, 1997, pp. 181–184.
48. L. Klapproth and G. Böck, Determination of the small-signal equivalent circuit elements from s-parameter measurements, *Conf. Proc., 8th Conf. Exhib. High Freq. Eng., Microw. Optron.,* 1995, pp. 423–427.
49. W. Daumann et al., InAlAs/InGaAs/InP HFET with suppressed impact ionization using dual gate cascode-devices, *IEEE Electron Device Lett.,* **17** (10): 488–490, 1996.
50. M. Schlechtweg et al., Coplanar millimeter-wave IC's for W-band applications using 0.15 μm pseudomorphic MODFET's, *IEEE J. Solid-State Circuits,* **31** (10): 1426–1434, 1996.
51. S. D. Personick, Receiver design for digital fiber optical communication systems, Pts. 1 and 2, *Bell Syst. Tech. J.,* **52**: 843–886, 1973.
52. S. van Waasen et al., 27 Ghz bandwidth high-speed monolithic integrated optoelectronic photoreceiver consisting of a waveguide fed photo-diode and an InAlAs/InGaAs-HFET-traveling wave amplifier, *IEEE J. Solid-State Circuits,* **32**: 1394–1401, 1997.
53. H.-G. Bach et al., Ultrafast monolithically integrated InP-based photoreceiver: OEIC-design, fabrication, and system application, *IEEE J. Sel. Top. Quantum Electron.,* **2** (2): 418–423, 1996.
54. R. M. Bertenburg, A. Clement, and F. J. Tegude, 40Gbit/s high sensitive optical receivers using photo detectors and TWAs: Design considerations and development, *Conf. Proc., Microw. Optron., 8th Exhib. Conf. High Freq. Eng. (MIOP-1995),* Sindelfingen, Germany, 1995, pp. 600–606.

M. Agethen
R. Reuter
T. Breder
R. M. Bertenburg
W. Brockerhoff
F. J. Tegude
Gerhard-Mercator University
Duisburg, Germany